

Surveying Diffusion in Complex Geometries. An Essay.

Denis S. Grebenkov

*Laboratoire de Physique de la Matière Condensée,
CNRS – Ecole Polytechnique, F-91128 Palaiseau, France
Email: denis.grebenkov@polytechnique.edu*

August 20, 2018

Abstract

The surrounding world surprises us by the beauty and variety of complex shapes that emerge from nanometric to macroscopic scales. Natural or manufactured materials (sandstones, sedimentary rocks and cement), colloidal solutions (proteins and DNA), biological cells, tissues and organs (lungs, kidneys and placenta), they all present irregularly shaped “scenes” for a fundamental transport “performance”, that is, diffusion. Here, the geometrical complexity, entangled with the stochastic character of diffusive motion, results in numerous fascinating and sometimes unexpected effects like diffusion screening or localization. These effects control many diffusion-mediated processes that play an important role in heterogeneous catalysis (reaction rate and overall production), biochemical mechanisms (protein search and migration), electrochemistry (electrode-electrolyte impedance), growth phenomena (solidification, viscous fingering), oil recovery (structure of sedimentary rocks), or building industry (cement hardening). In spite of a long and rich history of academic and industrial research in this field, it is striking to see how little we know about diffusion in complex geometries, especially the one which occurs in three dimensions.

We present our recent results on restricted diffusion. We look into the role of geometrical complexity at different levels, from boundary microroughness to hierarchical structure and connectivity of the whole diffusion-confining domain. We develop a new approach which consists in combining fast random walk algorithms with spectral tools. The main focus is on studying diffusion in model complex geometries (von Koch boundaries, Kitaoka acinus, etc.), as well as on developing and testing spectral methods. We aim at extending this knowledge and at applying the accomplished arsenal of theoretical and numerical tools to structures found in nature and industry (X-ray microtomography 3D scans of a cement paste, 2D slices of human skin and the placenta, etc.).

Preface

The essay is based on the author's research summary that has been prepared for defending a Habilitation degree (*Habilitation à Diriger des Recherches* in French). This is a structured overview of the author's works in different fields in which diffusion, geometry and complexity are entangled. As a summary of one scientist's activity, the essay is unavoidably biased and is not meant to provide a reader with a complete overview. Although the bibliography is extended, it certainly does not include all the references that are relevant for these research fields. In spite of this incompleteness, a reader may hopefully find interesting results and intriguing open problems for future research.

Contents

Introduction	4
1 Diffusion, geometry and complexity	6
1.1 Diffusion	6
1.2 Boundary condition	9
1.3 Reflected Brownian motion	10
1.4 Spectral analysis	12
1.5 Applications in NMR	12
1.6 Complexity and irregular geometry	15
2 Probabilistic insight: Monte Carlo simulations	16
2.1 Geometry-adapted fast random walks (GAFRW)	18
2.2 Multifractal properties of the harmonic measure	18
2.2.1 Multifractal analysis	20
2.2.2 Interpolation of the scale-dependent exponents	21
2.2.3 Harmonic measure in 3D	21
2.2.4 What makes a boundary less accessible?	22
2.3 Spread harmonic measures	23
2.3.1 Effect of spreading and exploration length	24
2.3.2 Scaling properties of the spread harmonic measures	24
2.4 First passage statistics on fractal boundaries	26
2.4.1 First passage statistics	26
2.4.2 Scaling relations	27
2.4.3 Numerical verification	28
2.5 Passivation processes	28
2.5.1 Iterative passivation process	30
2.5.2 Modification of the GAFRW algorithm	31
2.5.3 Comparison between 2D and 3D cases	32
2.6 Diffusion-weighted imaging of the lungs	34
2.6.1 The human pulmonary acinus and its modeling	34
2.6.2 Monte Carlo simulations accounting for magnetic field gradients	35
2.6.3 Diffusion in healthy and emphysematous acini	36
2.6.4 What is the role of a complex internal architecture?	36
Summary	37

3	Spectral insight: Laplacian eigenfunctions	38
3.1	Matrix formalism	38
3.1.1	Perturbative derivation	38
3.1.2	Moments	41
3.2	NMR survey of restricted diffusion	42
3.2.1	Simple geometries	42
3.2.2	Time-dependent diffusion coefficient	43
3.2.3	Different diffusion regimes	45
3.2.4	Rigorous results for relaxing boundaries	45
3.2.5	Cosine magnetic field in a slab	47
3.2.6	Diffusion in circular and spherical layers	48
3.3	Residence times of reflected Brownian motion	50
3.3.1	Local time on the boundary	52
3.3.2	Surface relaxation mechanism	53
	Conclusion	54
	Acknowledgments	55
	Bibliography	56

Introduction

Irregular shapes are ubiquitous in fields as different as biology, physiology, chemistry, electrochemistry, engineering, and material sciences. They play a crucial role in various natural phenomena and condition multiple industrial processes. For instance, a human being needs around hundred square meters of alveolar surface in the lungs for respiration. Since this surface has to fit the rib cage, it is necessarily irregular. Catalysts are often manufactured to have a rough boundary in order to increase the overall production because of a larger reactive surface. Oil-bearing sedimentary rocks and sandstones, cement and concretes, biological and textile tissues exhibit porous, often multiscale structures, in which transport processes take place. Either intrinsic or artificially implemented, a geometrical complexity essentially determines the properties and the overall functioning of an organ or an industrial device. Even for such a well-studied transport process as diffusion, an irregular geometry yields new, often unexpected phenomena. The central question of this work is *how a geometrical irregularity influences the dynamics of a complex system and, in turn, what information on geometry can be extracted from surveying this dynamics.*

We focus on diffusion for many reasons. First, it provides a reliable macroscopic framework for describing various microscopic dynamics according to the central limit theorem [1]. As such, diffusion turns out to be a fundamental transport mechanism in biology and chemistry. Second, diffusion is governed by a simple, though remarkably rich, second order partial differential equation (PDE) named diffusion (or heat) equation. Its interpretation in terms of Brownian motion provides the whole arsenal of powerful probabilistic tools as well as a basis for intuitive reasoning. Third, the spectral theory of the underlying Laplace operator is probably the most developed branch of functional analysis. Although diffusion is studied for a long time, the presence of a geometrical irregularity may drastically alter well-established results. As a matter of fact, it is striking to see how little we know about diffusion in complex geometries, especially the one which occurs in three dimensions. This is the reason for increasing interest in diffusion in recent decades.

Numerous questions and problems concerning diffusion in complex geometries can be formally divided in three groups:

- **forward problems** which consist in finding transport properties for a *known (defined) geometry* of a diffusion-confining domain. In mathematical terms, this is equivalent to finding a solution of the related PDE in this domain. More specifically, we are interested in finding a way to understand, both qualitatively and quantitatively, how various geometrical features of the confining domain change transport properties.
- **inverse problems** which aim at determining an *unknown geometry* of a diffusion-confining domain from measuring the transport properties of a system. This is the main purpose of imaging techniques. Diffusion-weighted nuclear magnetic resonance (NMR) imaging is an example. In this case, the magnetization attenuation which is caused by restricted diffusion in a porous medium is measured in order to get its global geometrical characteristics like surface-to-volume ratio, pore size distribution, etc. Kac's question "Can one hear the shape of a drum?" is the best illustration

of these issues [2]. Given their practical importance (e.g., in oil recovery or medical diagnosis), we shall bear in mind inverse problems in the course of this work.

- **optimization problems** which focus on conception and design of an *optimal geometry* to maximize or minimize certain transport characteristics of a system. The examples are efficient heat radiators, gas exchange units (e.g., filters), or catalysts, to name a few. Although we are not currently studying these questions, optimization problems are considered as an important direction for future research.

Throughout this work, we consider forward problems by adapting two approaches: Monte Carlo simulations and spectral analysis. As for Monte Carlo techniques, they prove to be efficient and very flexible tools for generating individual random trajectories of diffusing particles in complex geometries, including fractal boundaries, porous media, multiscale or branching structures, etc. (Section 2). As far as spectral analysis is concerned, it provides a fundamental explanation and a clearer interpretation of the observed effects (Section 3). The goal here is to relate various features of restricted diffusion to the Laplace operator eigenbasis and then to investigate the latter in depth. Since the numerical computation of the Laplace operator eigenbasis is a difficult task for complex geometries, we mainly focused on simple domains (e.g., interval, disk, sphere). For these, many characteristics of restricted diffusion can be found either analytically, or very accurately via spectral-oriented numerical techniques. As for complex geometries, their systematic study is one of the principal research lines in future.

The manuscript is organized as follows. Section 1 briefly summarizes physical concepts and mathematical tools for describing diffusion in complex media. We defined two principal research guidelines in order to present our main results: Monte Carlo simulations (Section 2) and spectral analysis (Section 3). All the author's publications are available online¹.

¹http://pmc.polytechnique.fr/pagesperso/dg/publi/publi_e.htm

1 Diffusion, geometry and complexity

1.1 Diffusion

Diffusion is a fundamental transport mechanism, with countless examples in nature and applications in sciences, from physics to biology, chemistry, medicine, engineering, and economics.

“Upscaling”: toward macroscopic (or PDE) description

The microscopic dynamics of gases and liquids can be described by kinetic theory, when a collision integral accounts for short-time and short-range interactions between atoms or molecules [3, 4]. From this classical point of view, the trajectory of a particle is a sequence of “moves” between successive “collisions” (or effective interactions) with other particles or a reservoir. In many cases, the mean free path is much shorter than macroscopic length scales at which the system is being observed. In addition, a large number of interactions considerably reduces or fully eliminates memory effects at macroscopic time scales, so that the specific motional features of the particle trajectory are averaged out. Performing such an “upscaling”, one aims to introduce a *macroscopic* density of particles and study its properties instead of looking at the *microscopic* dynamics of these particles. While the microscopic dynamics may be defiantly complex, its coarser macroscopic description is often appropriate and very accurate.

Diffusion equation

The diffusion (or heat) equation provides the simplest, though very general, coarser description of the microscopic dynamics:

$$\frac{\partial}{\partial t}c(\mathbf{r}, t) = D\Delta c(\mathbf{r}, t), \quad (1)$$

where $\Delta = \partial^2/\partial x_1^2 + \dots + \partial^2/\partial x_d^2$ is the Laplace operator in d dimensions, and D the free diffusion coefficient. This equation states that the evolution of the density of particles $c(\mathbf{r}, t)$ in time (the left-hand side term) is only caused by local displacements of particles in space (the right-hand side term). The differential form of this equation reflects the local character, in space and time, of the microscopic dynamics. If large moves were allowed during a short time, the Laplace operator Δ would be replaced by an integral operator accounting for particles coming from distant regions (spatially nonlocal macroscopic dynamics). If the microscopic moves were highly correlated, the time derivative $\partial/\partial t$ would be replaced by an integral operator accounting for the memory of the whole preceding evolution (temporarily nonlocal macroscopic dynamics). Although both situations can be encountered, we shall not consider such anomalous diffusions (see [5–10] and references therein).

Diffusive propagator

The diffusion equation describes the time evolution of the spatial density $c(\mathbf{r}, t)$ from a given initial state $c(\mathbf{r} = \mathbf{r}_0, t = 0) = \rho(\mathbf{r}_0)$. Among various initial conditions, a point-like source plays a special role. In fact, it is natural to ask how the density of particles started

from a given point \mathbf{r}_0 evolves? The family $G_t(\mathbf{r}_0, \mathbf{r})$ of these densities, parameterized by the starting point \mathbf{r}_0 , bears different names: diffusive propagator, heat kernel, or Green function of diffusion equation. These densities satisfy the diffusion equation with respect to \mathbf{r} ,

$$\left(\frac{\partial}{\partial t} - D\Delta\right) G_t(\mathbf{r}_0, \mathbf{r}) = 0, \quad (2)$$

with the initial condition for all particles to be concentrated in one point \mathbf{r}_0 which is mathematically represented by the Dirac distribution

$$G_{t=0}(\mathbf{r}, \mathbf{r}') = \delta(\mathbf{r} - \mathbf{r}'). \quad (3)$$

The symmetry property $G_t(\mathbf{r}, \mathbf{r}') = G_t(\mathbf{r}', \mathbf{r})$ holds.

The propagator is an elementary “block” describing the dynamics of particles at macroscopic level. As such, the propagator contains all the available information about diffusion. In particular, the solution $c(\mathbf{r}, t)$ of diffusion equation (1) with a given initial density $\rho(\mathbf{r}_0)$ is simply expressed through the propagator:

$$c(\mathbf{r}, t) = \int d\mathbf{r}_0 \rho(\mathbf{r}_0) G_t(\mathbf{r}_0, \mathbf{r}).$$

Extensions

Apart from the aforementioned global modifications (spatially or temporarily nonlocal dynamics), the diffusion equation (1) can be extended in many ways:

1. In anisotropic media, diffusion in some spatial directions may be faster or slower than in the others. This can be easily incorporated by adding weighting coefficients in front of the partial derivatives $\partial^2/\partial x_k^2$. In general, the Laplace operator can be replaced by a second-order elliptic differential operator,

$$\mathcal{D} = \sum_{i,j=1}^d a_{i,j}(\mathbf{r}) \frac{\partial^2}{\partial x_i \partial x_j}$$

where the coefficients $a_{i,j}(\mathbf{r})$ satisfy some requirements to ensure the ellipticity [11]. Clearly, this extension includes a spatially inhomogeneous diffusion coefficient. It is worth noting that many results for the Laplace operator relying on the spectral analysis are directly applicable to this extension. In what follows, we shall focus on the Laplace operator.

2. In some cases, the diffusion coefficient depends on time t or/and density $c(\mathbf{r}, t)$. The latter dependence may describe saturation effects in catalytic reactions. However, this dependence would make the diffusion equation nonlinear, significantly reducing the arsenal of analytical tools. For this reason, we shall not consider such extensions.
3. A bulk source or sink term can be added to the diffusion equation. Its practical implementation is straightforward, especially when using the spectral description.
4. An external scalar field $B(\mathbf{r}, t)$ can be included

$$\frac{\partial}{\partial t} c(\mathbf{r}, t) = D\Delta c(\mathbf{r}, t) - \kappa B(\mathbf{r}, t) c(\mathbf{r}, t), \quad (4)$$

where κ is a parameter. The last term accounts for the local effects: loss or production of the particles, modification of their state, etc. The proportionality to the density $c(\mathbf{r}, t)$ reflects that these local effects act on each particle individually and independently from the other particles. The second and higher-order powers of the density may represent various chemical reactions, but we shall not consider these nonlinear equations.

Depending on the application field, $B(\mathbf{r}, t)$ incorporates various mechanisms. If the bulk contains absorbing sinks or traps for diffusing particles, $B(\mathbf{r}, t)$ represents the distribution of their absorption or trapping rates. If the particles possess some activity function which can relax on bulk impurities (e.g., a magnetization of a polarized spin carried by a diffusing nucleus), $B(\mathbf{r}, t)$ describes bulk relaxation rate. If the particles can be chemically transformed by catalytic germs (or biological cells) distributed in the bulk, $B(\mathbf{r}, t)$ characterizes the distribution of reaction rates. In NMR, $B(\mathbf{r}, t)$ with imaginary parameter κ represents the effect of the applied magnetic field onto the transverse magnetization (Sect. 1.5). In what follows, our main focus will be onto Eq. (4).

“Downscaling”: toward probabilistic description

In a coarser description via diffusion equation, all the information about individual trajectories of the particles is lost. Nevertheless, thinking of diffusion in terms of individual particles can still be instructive to better understand or interpret various characteristics of diffusion. As we already mentioned earlier, the real microscopic dynamics is in general very complicated and intractable analytically. To overcome this problem, one employs the concept of “downscaling” which consists in finding a simpler *microscopic* dynamics that would lead to the chosen *macroscopic* description. A Brownian motion, mathematically defined as a stochastic process with independent Gaussian increments [1], is a very natural candidate for substituting the real microscopic dynamics. In fact, the diffusive propagator $G_t(\mathbf{r}_0, \mathbf{r})$, satisfying Eqs. (2, 3), turns out to be the probability density for Brownian motion to move from \mathbf{r}_0 to \mathbf{r} during time t . This is a direct link between probabilistic and PDE descriptions. Strictly speaking, this “substitution” is neither unique, nor physically justified. It is rather a useful model that offers efficient probabilistic tools for theoretical and numerical analysis. In particular, random walks on a lattice (a discretized version of Brownian motion) are broadly employed to model many physical processes [12, 13].

Feynman-Kac formula

In practice, it is difficult to monitor the individual Brownian trajectories of the diffusing particles. It is much easier to measure or investigate “an observable”, or a functional, of these trajectories. We consider the random variable

$$\varphi = \int_0^t dt' B(X_{t'}, t - t'), \quad (5)$$

where Brownian motion is started with a given initial density $\rho(\mathbf{r}_0)$. Intuitively, a given function $B(\mathbf{r}, t)$ can be thought of as a distribution of “markers” to “color” the trajectory X_t exploring different points or specific regions in space. When the diffusing species

passes through these regions, the random variable φ accumulates the corresponding marks. In other words, different parts of the trajectory are weighted according to the function $B(\mathbf{r}, t)$, encoding thus the whole stochastic process. For example, if $B(\mathbf{r}, t)$ represents the distribution of absorption or relaxation rates in the bulk, φ is the cumulant absorption factor penalizing the trajectories that pass through the sinks or traps. In NMR, the encoding mechanism is experimentally realized by applying an inhomogeneous magnetic field $B(\mathbf{r}, t)$, and φ is the total phase accumulated by an individual spin-bearing particle during its diffusion in this field [14].

Since φ is a random variable, it is convenient to consider the Fourier or Laplace transform of its probability distribution which can be respectively interpreted as characteristic function $\mathbb{E}\{e^{iq\varphi}\}$ and survival probability $\mathbb{E}\{e^{-\kappa\varphi}\}$. The Feynman-Kac formula relates these probabilistic quantities to the solution of Eq. (4)

$$\mathbb{E}\{e^{-\kappa\varphi}\} = \int d\mathbf{r} c(\mathbf{r}, t) \quad (6)$$

(if κ is replaced by $-iq$, one obtains the characteristic function) [15–19]. In what follows, we shall frequently employ this relation to “switch” between probabilistic and PDE representations. In particular, the probabilistic description suggests using Monte Carlo simulations for solving PDE problems [20–22]. We shall consider various applications of this numerical technique in Section 2.

1.2 Boundary condition

When the motion of diffusing species is restricted inside a confining medium, physico-chemical or biological interactions between the particles and the interface of the medium should be taken into account. For instance, paramagnetic impurities dispersed on the interface cause surface relaxation in NMR experiments; cellular membranes allow for a semi-permeable transport through the boundary; chemical reaction may change the diffusive or magnetic properties of the particle, etc. A reliable description of these processes at microscopic level is a challenging problem, demanding for example accurate molecular dynamics simulations near the interface, or quantum mechanics calculations. At the time scale of the macroscopic transport process, however, the contact with the interface is very rapid so that the precise description of the interaction is often irrelevant. In analogy with diffusion coefficient D , effectively representing the bulk dynamics, the interactions on the boundary can macroscopically be described by a surface transport coefficient W [23, 24]. In microbiology, this is the permeability characterizing the rate of transfer across a semi-permeable membrane. In heterogeneous catalysis, W is the reactivity of a catalyst, that is the rate at which diffusing species are chemically transformed into other species after hitting the catalytic surface. In NMR, W is the surface relaxivity determining the rate at which the nuclei lose their magnetization in the vicinity of the boundary. In the two latter cases, the transformed or relaxed species still remain inside the confining domain but they do not participate at the transport process any more (e.g., they do not contribute to formation of the macroscopic signal, see Sect. 1.5).

At macroscopic level, interactions with the interface are effectively incorporated via a boundary condition, which is a mass conservation law: the flux of particles from the bulk *towards* the boundary, $-D\partial c(\mathbf{r}, t)/\partial n$, is equal to the flux *through* the boundary (or the

flux of transformed or relaxed species) $Wc(\mathbf{r}, t)$, yielding Robin (also known as Fourier, mixed, relaxing, radiative, or third) boundary condition

$$D\frac{\partial}{\partial n}c(\mathbf{r}, t) + Wc(\mathbf{r}, t) = 0, \quad (7)$$

where $\partial/\partial n$ is the normal derivative pointing outward the bulk (if the domain is a sphere, the normal derivative is equal to the radial derivative). When the surface transport coefficient W is zero (no flux through the boundary), one retrieves Neumann boundary condition: $\partial c(\mathbf{r}, t)/\partial n = 0$. The opposite limit of infinite W (no resistance to the transfer through the boundary) yields Dirichlet boundary condition: $c(\mathbf{r}, t) = 0$. The intermediate Robin boundary condition is a linear combination of these two extreme cases, which are “weighted” by bulk and surface transport coefficients D and W , respectively. In other words, the ratio D/W represents “proportions” of pure reflections (the first term) and pure absorptions (the second term), mixing Neumann and Dirichlet boundary conditions.

The role of Robin boundary condition for Laplacian transport was thoroughly investigated (see [23, 24] and references therein). In particular, the ratio D/W , which is homogeneous to a length, bears different names: “unscreened perimeter length” or “exploration perimeter or length” [25], “Damköhler first ratio” in chemistry [26], “surface relaxation length” in NMR [27]. In the latter case, D/W is the distance a particle should travel near the boundary before surface relaxation reduces its expected magnetization. In Sect. 2.3, we shall give another interpretation to this exploration perimeter.

1.3 Reflected Brownian motion

In the above macroscopic description, restricting walls of a confining medium were introduced through boundary conditions for diffusion equation. Alternatively, this effect can be incorporated for Brownian motion in the probabilistic description. We first consider a much simpler situation of fully absorbing interface (Dirichlet boundary condition). For a Brownian motion W_t started from a point \mathbf{r}_0 inside a confining domain Ω , we define the first hitting time \mathbb{T} when W_t reaches the boundary $\partial\Omega$ of Ω :

$$\mathbb{T} = \inf\{t > 0 : W_t \in \partial\Omega\}. \quad (8)$$

Since the interface is fully absorbing, the process is stopped (or killed) at this (random) moment. Figuratively speaking, we simply “close our eyes” on what happens with Brownian motion after \mathbb{T} . It is relatively easy to incorporate Dirichlet boundary condition by restricting the analysis to times t inferior to \mathbb{T} .

The situation with a reflecting interface (Neumann boundary condition) is completely different. In this case, one needs to keep Brownian motion inside the confining domain without stopping it. In other words, we have to modify the local dynamics of this process to include reflections on the boundary. In sharp contrast with ordinary Brownian motion, the construction of reflected Brownian motion strongly depends on the geometry of a confining medium, being especially sophisticated for irregular boundaries. The simplest example of this process is the absolute value of a one-dimensional Brownian motion W_t : $X_t = |W_t|$. Each time a diffusing particle crosses the boundary of the positive semi-axis (the end point 0), it is reflected toward the bulk (positive semi-axis). In a general situation of a bounded domain $\Omega \subset \mathbb{R}^d$ with twice continuously differentiable boundary

$\partial\Omega$, reflected Brownian motion X_t can be defined as a solution of the stochastic differential equation, called Skorokhod equation [17]:

$$dX_t = dW_t + \mathbf{n}(X_t)\mathbb{I}_{\partial\Omega}(X_t)d\ell_t,$$

where W_t is the (ordinary) Brownian motion, $\mathbf{n}(\mathbf{r})$ the normal inward vector at boundary point \mathbf{r} , $\mathbb{I}_{\partial\Omega}(\mathbf{r})$ the indicator function of the boundary ($\mathbb{I}_{\partial\Omega}(\mathbf{r}) = 1$ if $\mathbf{r} \in \partial\Omega$, and 0 otherwise), and ℓ_t the local boundary time process, satisfying certain conditions [17]. The most unusual feature of this definition is that the single equation defines two processes, X_t and ℓ_t , strongly dependent on each other. The intuitive meaning of the Skorokhod equation is simple. In the bulk, an infinitesimal variation dX_t of the reflected Brownian motion inside the confining domain is only governed by the variation dW_t of the (ordinary) Brownian motion (the second term vanishes due to the indicator function $\mathbb{I}_{\partial\Omega}$). When the particle hits the boundary, the second term does not allow to leave the domain leading to a variation directed along the inward unit normal $\mathbf{n}(\mathbf{r})$ towards the interior of the domain. At the same time, each encounter with the boundary increases the local time ℓ_t . Being defined in this way, reflected Brownian motion can be related to diffusion equation with Neumann boundary condition. It is worth noting that reflected Brownian motion can alternatively be introduced as a continuous limit of reflected random walks on a regular lattice, which are easier for intuitive interpretation [28, 29]. We also mention that reflected Brownian motion can be rigorously defined for domains with irregular boundaries using the Dirichlet form method [30, 31].

In the intermediate case of partially absorbing/reflecting interface (Robin boundary condition), one can introduce “partially reflected Brownian motion” [32]. This is reflected Brownian motion which is conditioned to stop (i.e., to be absorbed) on the boundary at random moment \mathbb{T}_h when the local time ℓ_t exceeds an independent exponentially distributed random variable ξ :

$$\mathbb{T}_h = \inf\{t > 0 : \ell_t \geq \xi\}, \quad \text{where } \mathbb{P}\{\xi > \lambda\} = \exp[-\lambda h].$$

The absorption can happen whenever partially reflected Brownian motion hits the boundary, these hits being counted by the local time. A positive parameter h , a kind of absorption rate, is actually the ratio between the surface and bulk transport coefficients, $h = LW/D$, L being a characteristic size of the domain to get rid off the dimensional units. In turn, the exponential character of the random “threshold” ξ is related to the fact that the absorption event is independent from hit to hit (as the exponential decay of radioactive nuclei).

When h goes to infinity (Dirichlet boundary condition, $W = \infty$), one gets $\xi = 0$ with probability 1, so that the stopping time T_∞ describes the first moment when the local time ℓ_t exceeds 0. This is exactly the moment when partially reflected Brownian motion hits the boundary for the first time. One thus retrieves the above definition (8) for a purely absorbing boundary. In the opposite limit $h \rightarrow 0$, $\xi = \infty$ with probability 1, yielding Neumann boundary condition ($W = 0$) as expected. Varying h allows one to explore various situations between pure absorptions and pure reflections that makes partially reflected Brownian motion to be a rich and flexible microscopic model for diffusive transport.

1.4 Spectral analysis

To the diffusion (or heat) equation is associated a set of solutions for a given confining domain. A particular solution is fixed by setting the initial condition. On the other hand, one can remain in a general frame and study the diffusion equation or, equivalently, the Laplace operator. In this so-called spectral approach, one is searching for the Laplacian eigenfunctions and eigenvalues. Instead of looking for one particular solution, one aims to find all the “relevant” solutions at once. It is not therefore surprising that the computation of the eigenbasis, fully describing the operator, is a difficult task. But once it is worked out, any solution of diffusion equation and any property related to the Laplace operator can be deduced.

The eigenfunctions $u_m(\mathbf{r})$ and eigenvalues λ_m of the Laplace operator Δ in a bounded domain Ω are defined as

$$\Delta u_m(\mathbf{r}) + \lambda_m u_m(\mathbf{r}) = 0 \quad (\mathbf{r} \in \Omega), \quad (9a)$$

$$D \frac{\partial}{\partial n} u_m(\mathbf{r}) + W u_m(\mathbf{r}) = 0 \quad (\mathbf{r} \in \partial\Omega), \quad (9b)$$

with an integer index $m = 0, 1, 2, \dots$. The eigenvalues λ_m are nonnegative, the eigenfunctions $u_m(\mathbf{r})$ are orthogonal:

$$\int_{\Omega} d\mathbf{r} u_m(\mathbf{r}) u_{m'}^*(\mathbf{r}) = \delta_{m,m'}, \quad (10)$$

where the asterisk denotes complex conjugate, and $\delta_{m,m'}$ is the Kronecker symbol ($\delta_{m,m'} = 1$ for $m = m'$, and 0 otherwise). Note that we explicitly fixed the normalization in Eq. (10).

The diffusive propagator has the following spectral decomposition [33–35]

$$G_t(\mathbf{r}, \mathbf{r}') = \sum_m u_m^*(\mathbf{r}) u_m(\mathbf{r}') e^{-D\lambda_m t}. \quad (11)$$

One can easily check that this sum satisfies the diffusion equation (2), while the initial condition (3) at $t = 0$ is guaranteed by the completeness relation

$$\delta(\mathbf{r} - \mathbf{r}') = \sum_m u_m(\mathbf{r}) u_m^*(\mathbf{r}').$$

At last, the boundary condition for the diffusive propagator follows immediately from Eq. (9b).

It is clear that eigenfunctions and eigenvalues explicitly determine the diffusive propagator. The opposite is also true: the propagator can be formally used to define the eigenfunctions and eigenvalues. In fact, the same amount of information about diffusive motion is “stored” differently in the eigenbasis and in the propagator, the latter mixing this information in a specific way.

1.5 Applications in NMR

Observation of translational dynamics requires a kind of “marking” or “labeling” of the traveling particles for tracking their displacements in space. A magnetic field is a superb

experimental tool for encoding the motion of spin-bearing particles. For nuclei with spin $1/2$ (e.g., protons of water), the magnetic field induces energy splitting into two levels. At thermal equilibrium, the population of the nuclei at the lower energy (i.e., the spins parallel with the magnetic field) is bigger than the population of the nuclei at the higher energy (i.e., the spins antiparallel with the magnetic field). The difference in these populations creates local magnetization which is parallel with the magnetic field (conventionally, the z axis). This magnetization can be flipped into the transverse xy plane by a 90° radio-frequency (rf) magnetic field pulse (Fig. 1). The spins at position \mathbf{r} start to precess with the Larmor frequency $\gamma B(\mathbf{r}, t)$ which is proportional to the magnetic field $B(\mathbf{r}, t)$, γ being the gyromagnetic ratio (a fundamental constant of the nucleus). The use of a spatially inhomogeneous magnetic field allows one to distinguish points or regions in space, as the nuclei precess faster or slower in different regions. This mechanism is widely applied in experiments to monitor the translational dynamics and to access the geometry of a confining medium [36].

The x and y projections of the transverse magnetization are conventionally treated as real and imaginary parts of a complex-valued “density” $c(\mathbf{r}, t)$. The magnetic-field encoding is then incorporated through Eq. (4) with an *imaginary* parameter $\kappa = i\gamma$, the last term in this equation being responsible for describing precession of the transverse magnetization. This equation, known as Bloch-Torrey equation [37], describes the evolution of $c(\mathbf{r}, t)$ according to two independent mechanisms

- diffusive migration of the spin-bearing particles (from \mathbf{r} to neighboring points), represented by the Laplace operator and characterized by the free diffusion coefficient D ;
- magnetic field encoding, when the spins at \mathbf{r} acquire the phase shift $\gamma B(\mathbf{r}, t)\tau$, resulting from their precession in the transverse plane during a short time τ .

The macroscopic signal at time t is formed by the whole ensemble of the spins diffusing inside the confining domain Ω :

$$E = \int_{\Omega} d\mathbf{r} c(\mathbf{r}, t) \tilde{\rho}(\mathbf{r}), \quad (12)$$

where $\tilde{\rho}(\mathbf{r})$ is a sampling or pickup function of the measuring coil or antenna (usually one tries to get $\tilde{\rho}(\mathbf{r})$ as uniform as possible). In analogy to Feynman-Kac formula (6), the signal can alternatively be written as the characteristic function $\mathbb{E}\{e^{i\gamma\varphi}\}$ of the random dephasing φ of an individual nucleus diffusing in an applied magnetic field $B(\mathbf{r}, t)$ (the sampling function $\tilde{\rho}(\mathbf{r})$ being implicitly incorporated here in the expectation). Both formulations are widely used in NMR literature (see [14] and references therein).

In most practical situations, the encoding term $B(\mathbf{r}, t)$ is a superposition $B_0 + f(t)(\mathbf{g} \cdot \mathbf{r})$ of a static magnetic field B_0 and a linear magnetic field gradient \mathbf{g} , whose dependence on time is represented through a dimensionless temporal profile $f(t)$. The form of the temporal profile can be easily varied in modern MR scanners. The simplest choice $f(t) = 1$ corresponds to a free induction decay (FID) in a constant gradient. Two identical gradient pulses of opposite directions can be applied to form a gradient echo. If the nuclei were immobile, their dephasing by the first gradient pulse would be fully compensated by the second gradient pulse. When the nuclei diffuse, they experience various magnetic

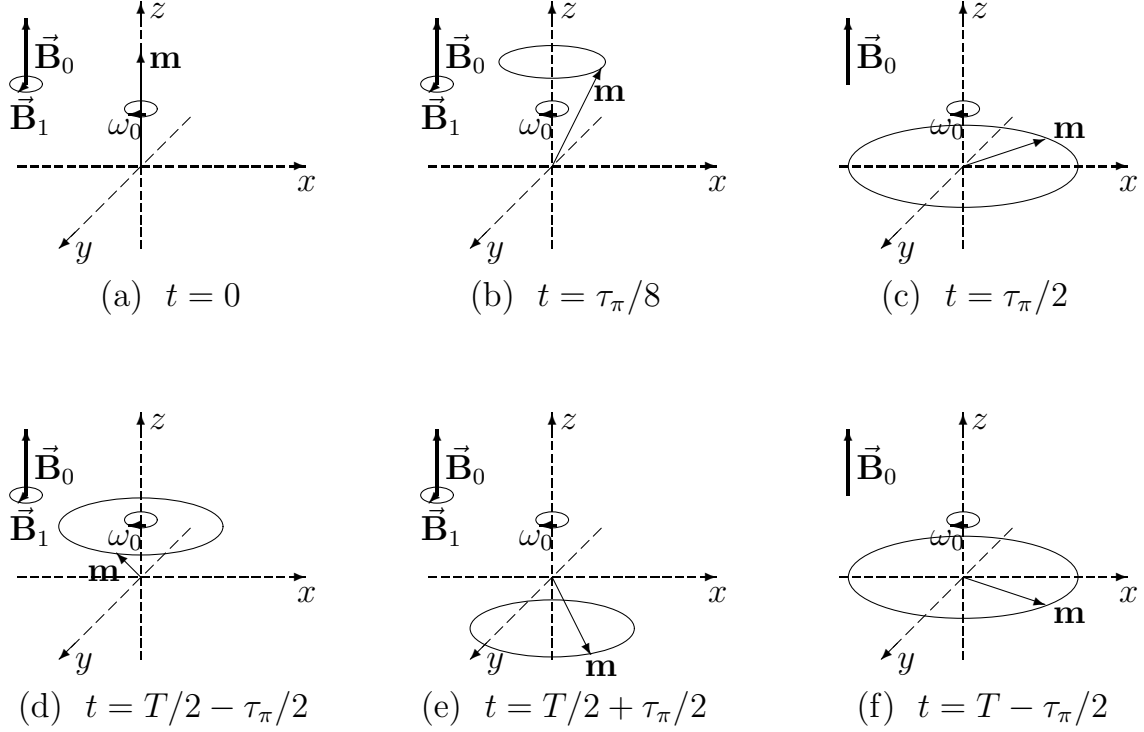


Figure 1: Schematic illustration of echo formation. In a static field B_0 along the z axis, the spins precess around this axis with the Larmor frequency $\omega_0 = \gamma B_0$, and its magnetization \mathbf{m} is directed along z . (a) At time $t = 0$, one applies a periodic magnetic field B_1 rotating in the transverse plane xy with frequency ω_0 (so-called $\pi/2$ or 90° radio-frequency (rf) pulse). (b) Still precessing, the magnetization is turning, linearly in time, toward the transverse plane. (c) At $t = \tau_\pi/2$ (here $\tau_\pi = \pi/(\gamma B_1)$), the magnetization lies in the transverse plane, and the periodic magnetic field B_1 ceases. During the following period $\Delta T = T/2 - \tau_\pi$, the magnetization slowly relaxes back to the longitudinal direction (axis z). (d) At $t = T/2 - \tau_\pi/2$, another magnetic field pulse is applied during the time τ_π (so-called π or 180° rf pulse). (e) This pulse inverts the longitudinal direction of the magnetization. (f) After the 180° rf pulse being turned off at $t = T/2 - \tau_\pi/2$, the slow relaxation during the subsequent time period ΔT returns the magnetization into the transverse plane. Moreover, the magnetizations of various spins are refocused thus forming a macroscopic signal (an echo) at $t = T - \tau_\pi/2$. The rf pulses are very short allowing their durations ($\tau_\pi/2$ and τ_π) to be neglected. When the magnetic field is spatially inhomogeneous, the refocusing is not complete because the spins, precessing with varying Larmor frequencies, acquire different phase shifts. The resulting macroscopic signal depends on translational dynamics of spins, allowing one to survey this dynamics in an experiment.

fields and dephase differently. As a consequence, the rephasing is not complete, and the gradient-echo amplitude attenuation characterizes restricted diffusion (see below).

Measuring the macroscopic signal E as a function of the experimentally controlled parameters (gradient, diffusion time, temporal profile, etc.), one aims to retrieve as much information on the dynamics and the geometry of confinement as possible. Solving this inverse problem necessarily requires knowing how a given geometry influences the macroscopic signal. This forward problem will be considered throughout the manuscript.

1.6 Complexity and irregular geometry

The diffusion (or heat) equation and the underlying spectral analysis of the Laplace operator in a bounded domain is a classical problem in mathematics [34, 35]. What is new in our consideration of this old problem is *an irregular geometry* of a medium or its boundary. As a matter of fact, porous materials, concentrated colloidal suspensions, and physiological organs (such as lungs or kidneys) are examples of systems developing large specific surfaces. They all present a rich variety of shapes and exhibit complex morphologies on a wide range of length scales. In these systems, the interfacial confinement strongly influences the diffusive dynamics of Brownian particles.

The human lung is a striking example of a complex transport system, in which the irregular geometry plays a central role. Its branching structure guarantees a rapid access of a large quantity of fresh air towards thirty thousands of pulmonary acini [38]. Each acinus is a porous, dichotomously branched gas exchange unit, in which oxygen molecules diffuse toward the alveolar membranes for further transfer to the blood. The complexity of this geometry was shown to lead to diffusion screening, one of the physical mechanisms for regulating the physiological efficiency of the lungs [25]. Many other physiological organs (such as kidneys, intestine, placenta) have also hierarchical multiscale structure. Moreover, biological systems often present geometrical complexity even at microscopic scales (like the surface of cells [39]).

In material sciences, multiscale porous structures are as well ubiquitous. Typical examples are: sedimentary rocks, clays, sandstones, plasters, cement, etc. For instance, the geometrical structure of a cement paste is responsible for mechanical strength and the overall resistance of buildings, while its alteration in time by diffusion-mediated reactions is a major reason for aging, cracks, failures or even collapses [40]. A large part of worldwide reserve of crude oil is “imprisoned” in sedimentary rocks, and their porous morphology is a key factor for oil recovery [41]. A microroughness of metallic electrodes (scratches, abrasions, etc.) may substantially alter their transport properties and functioning [42]. Finally, the tortuous surface of proteins and DNA molecules, when looked at microscopic scales, is relevant for diffusion-mediated biochemical reactions. At a larger scale, industrial catalysts are made of very irregular shape to increase the catalytic surface aiming to improve the overall production rate [43].

In summary, irregular shapes are encountered in nature and sciences more often than one usually expects. These irregularities span a wide range of length scales (from nanometers to hundreds of meters) and exist in a variety of systems, from biology to mineral sciences. The diffusive motion of particles inside such a medium is substantially influenced by its complex geometry. This is a major research topic of this manuscript.

2 Probabilistic insight: Monte Carlo simulations

In physics, speaking about diffusion in complex geometries invokes numerical analysis by default. In fact, only for few simple shapes (such as a disk or a sphere), diffusion equation possesses explicit solutions. All other domains require solving diffusion equation on a computer. A variety of numerical methods can be roughly divided into two groups.

In the first group (finite differences, finite elements, boundary elements, etc.), a domain and/or its boundary is discretized with a regular or adaptive mesh. The original continuous problem is then replaced by a set of linear equations to be solved numerically. The solution $c(\mathbf{r}, t)$ is obtained at all mesh nodes at successive time moments. Since the accuracy and efficiency of these deterministic numerical schemes significantly rely on the discretization, mesh construction for complex geometries turns out to be the key issue and often a limiting factor, especially in three dimensions.

In the second group (Monte Carlo simulations), a probabilistic interpretation of PDE is employed. Solving the original continuous problem is replaced by modeling random trajectories of the underlying diffusion process. The solution is then obtained via Feynman-Kac formulas (Eq. (6) or similar) by averaging over random trajectories. Since there is no discretization neither of the domain, nor of boundary conditions (the most subtle stage for the first group), Monte Carlo techniques are in general flexible and easy to implement. Two drawbacks should however be mentioned: a slow convergence to the solution (error typically decreases as $1/\sqrt{N}$, N being the number of the simulated trajectories) and the local character of simulations (the solution is obtained at one spatial point). For this latter reason, Monte Carlo simulations are not well appropriate for getting the whole solution $c(\mathbf{r}, t)$. In contrast, this drawback is removed when one is interested in some average of the solution like, for instance, in Eq. (12). As illustrated in this Section, Monte Carlo techniques become particularly well suited, especially for studying diffusion in complex geometries.

Monte Carlo simulations

In the simplest case, one fixes a small time step τ and generates a stochastic trajectory X_t from a chosen starting point x_0 by adding successively random increments ξ_n :

$$X_0 = x_0, \quad X_{(n+1)\tau} = X_{n\tau} + \xi_n \quad (n \geq 0).$$

For Brownian motion, all the increments are independent identically distributed random variables with normal (Gaussian) law, with mean zero and standard deviation $\sigma = \sqrt{2D\tau}$ (an extension to the multidimensional case is straightforward). A discretized version of this process is obtained by taking $\xi_n = \pm\sigma$ with randomly chosen sign. These are random walks on a lattice with mesh σ . Restricting walls can be taken into account either by stopping the process after their hit (Dirichlet boundary condition), or by reflecting the particle inside the domain (Neumann boundary condition), or by a combination of both (Robin boundary condition).

Given the simplicity of this procedure, its implementation is easy for various domains, but its practical applications are in general limited to simple geometries. In fact, an accurate modeling of the trajectory requires to keep a typical step σ (or the lattice mesh) smaller than the smallest geometrical feature of a confining domain. Since complex geometries (e.g., fractals) are often multiscale, the distances that should be explored by

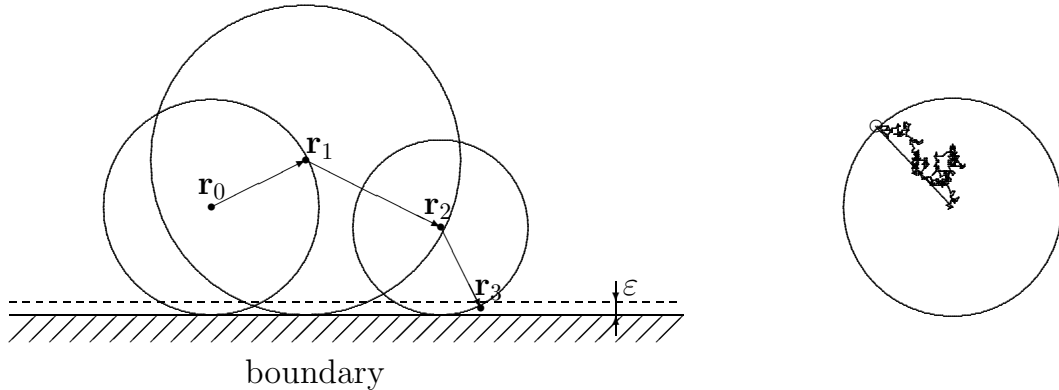


Figure 2: Illustration of a fast random walk algorithm. From the current position, one determines the distance to the boundary (here, for a flat horizontal segment, it is the height of the current point above the boundary) and draws the circle (or a sphere in 3D). One then chooses a uniformly distributed random point on this circle and makes the jump. From this new position, one repeats the above steps, generating a sequence of points $\mathbf{r}_0, \mathbf{r}_1, \mathbf{r}_2, \dots$, until the particle approaches the boundary closer than a chosen threshold ε . At this point, the simulation stops and the particle is considered as having hit the boundary. As illustrated on the right, each jump replaces a Brownian path inside the circle that speeds up simulations considerably.

diffusing particles inside the confining domain are by orders of magnitude longer than its smallest geometrical features, requiring very long and time-consuming simulations for a single trajectory.

To overcome this difficulty, Muller proposed to replace Brownian motion by an equivalent “spherical process” [44]. This method, often called “fast random walks”, was employed by many authors (see, e.g., [45–47]). The idea is to explore a confining domain as fast as possible, without violating probabilistic properties of Brownian motion. Starting from a given point, a diffusing particle executes a series of random jumps in the bulk. The jump length at each step is taken to be the distance ℓ between the current position and the boundary (Fig. 2). Since the sphere (or the disk in 2d) of radius ℓ centered at the current position resides in the interior of the confining domain, Brownian motion inside this sphere is not altered by the presence of the restricting walls. Figuratively speaking, a diffusing particle can “see” only a close neighborhood of its current position so that it simply does not “know” about the walls far away. The continuity of Brownian motion implies that the diffusing particle must intersect somewhere the frontier of this sphere before hitting the boundary. The rotational symmetry yields the uniform distribution of intersection points. It means that a lengthy simulation of Brownian trajectory inside the sphere can be replaced by a single random jump from its center to a uniformly distributed point on its frontier (Fig. 2). This “trick” drastically speeds up Monte Carlo simulations since at each step the largest possible exploration is performed.

In practice, the computation is reduced to finding the distance from any interior point to the boundary. Depending on the studied geometry, this problem can be solved in different ways. In the next subsection, a geometry-adapted fast random walks (GAFRW) algorithm is presented.

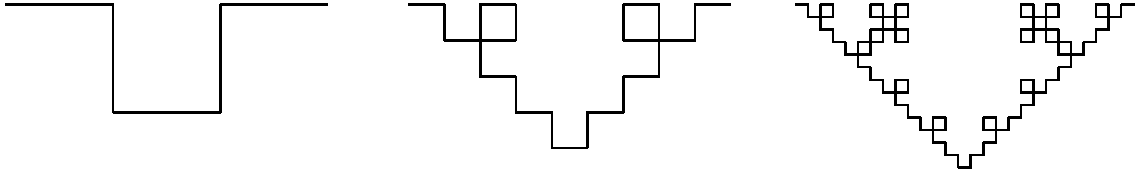


Figure 3: Three generations of the quadratic von Koch curve of fractal dimension $D_0 = \ln 5 / \ln 3 \approx 1.465$. At each iteration, one replaces all linear segments by the rescaled generator (first generation).

2.1 Geometry-adapted fast random walks (GAFRW)

Fractals are often used as a paradigm of complex domains [48–51]. On one hand, fractals are very irregular shapes which exhibit geometrical details at various length scales, “exploding” the classical notions of length, surface area or volume. On the other hand, self-similar or self-affine hierarchical structures help to perform accurate theoretical and numerical analysis on fractals. In particular, the self-similarity of von Koch curves and surfaces allowed us for a rapid computation of the distance from any interior point to these boundaries [52].

To illustrate these ideas, we consider the quadratic von Koch curve (Fig. 3). When a random walker is far from the boundary, it does not “distinguish” its geometrical details. One can thus estimate the distance by considering the coarsest generation (Fig. 4). Getting closer and closer to the boundary, the random walker starts to recognize smaller and smaller geometrical details. But at the same time, when small details appear in view, the rest of the boundary becomes “invisible”. Consequently, one can explicitly determine the distance by examining only the local geometrical environment (see [52] for details).

When the particle approaches the boundary closer than a chosen threshold, we say that it hits the boundary. Depending on the boundary condition and the problem at hand (see below), the particle is either absorbed (simulation is stopped), or reflected (simulation is resumed from a nearby bulk point).

An advantage and eventual drawback of this GAFRW algorithm is the need for a specific implementation for each studied geometry. The algorithm was developed for the above quadratic von Koch curve and the cubic von Koch surface of fractal dimension $D_0 = \ln 13 / \ln 3$, as well as for triangular von Koch curves of variable fractal dimension (Sect. 2.2.4). In the next subsections, we shall discuss various applications of this algorithm.

2.2 Multifractal properties of the harmonic measure

The initial purpose for developing GAFRW algorithm was for studying the accessibility of a boundary to diffusing particles, which is of primary importance in growth and transport phenomena. Actually, the transfer or reactive capacity of an interface is crucially limited by its accessibility for Brownian motion, the effect known as diffusion screening (similar to electric screening in electrostatics). A particle diffusing towards an irregular interface has very little chance to reach the bottom of a deep “fjord” before hitting more prominent (and easier accessible) points. The resulting distribution of diffusive fluxes or arrival probabilities on the boundary is therefore very uneven, a small fraction of the boundary

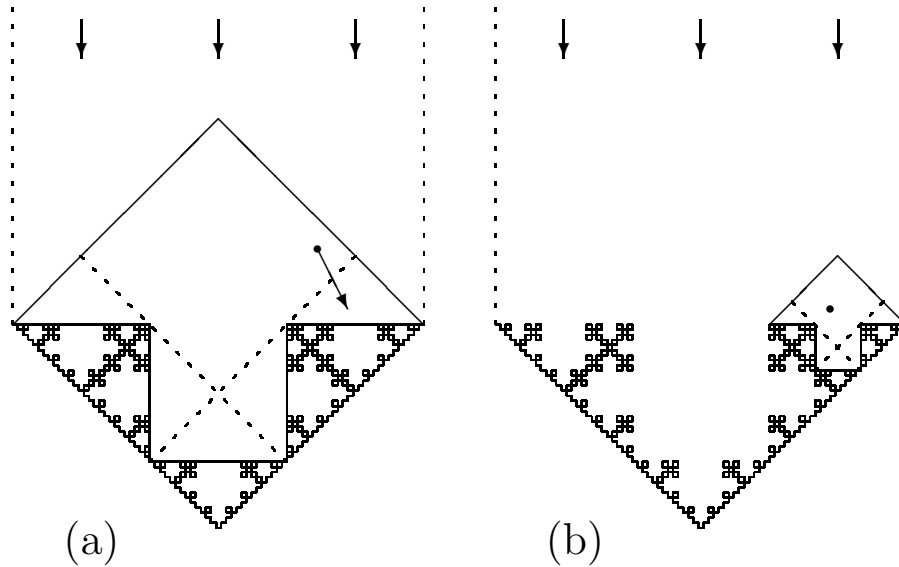


Figure 4: Basic arrow-like cell which is divided into the rotated square and five small triangles (a). Once a Brownian particle arrived into the rotated square, the distance between its current position (full circle) and the boundary of the arrow-like cell (the generator) can be computed explicitly. Random jumps inside the rotated square can therefore be executed, until the Brownian particle either exits from the arrow-like cell, or enters into a small triangle. In the latter case, the Brownian particle starts to “see” the geometrical details of the next generation. The rescaled arrow-like cell (b) is then used to compute the distance to the boundary. Note that a distant source is placed on the top of the figure, while two vertical dotted lines delimit the interior of the confining domain.

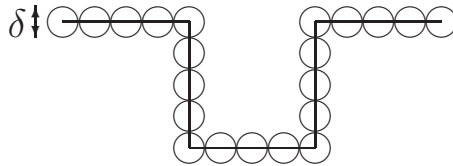


Figure 5: A given boundary (here, the first generation of the quadratic von Koch curve) is covered by disks of diameter δ .

receiving the overwhelming majority of the diffusing particles. The diffusion screening limits the overall production of species in the diffusion-limited regime of heterogeneous catalysis but allows one to design long-working catalysts [43].

Mathematically, this accessibility is characterized by a harmonic measure, which is defined for each (Borel) subset of the boundary as the probability for Brownian motion to reach the boundary of the confining domain for the first time at this subset [53]. This measure governs random growth processes (e.g., diffusion-limited aggregation, dendritic growth, solidification, viscous fingering, morphogenesis), primary current distribution in electrochemistry, distribution of particle flows on a membrane, electric charge distribution on a metallic surface, etc.

2.2.1 Multifractal analysis

For a smooth boundary, the harmonic measure is fully characterized by its density. When the boundary is irregular (e.g., fractal), there is no density, though the harmonic measure is still well defined. In this case, one uses the multifractal dimensions D_q of the harmonic measure to characterize its variations over different length scales.

Let a finite generation g of a fractal boundary be covered by disjoint compact sets of diameter δ (e.g., disks, spheres, cubes), as illustrated in Fig. 5. The harmonic measure at the scale δ is represented by a finite set of hitting probabilities $p_{k,\delta,g}$. The variation of the harmonic measure with the scale δ can be characterized by the behavior of the moments

$$\zeta(q, \delta, g) = \sum_k (p_{k,\delta,g})^q. \quad (13)$$

When δ goes to 0, $\zeta(q, \delta, g)$ scales as $\delta^{(q-1)D_q}$. For a smooth d -dimensional boundary, all the D_q are trivially equal to d , independently of the real parameter q . Geometrical irregularities may lead to different scaling of the harmonic measure for various q . Except for few classes of fractals [54–56], the multifractal dimensions of the harmonic measure need to be determined numerically. The GA FRW algorithm was used to simulate Brownian trajectories from a distant source toward von Koch boundaries and to calculate approximately the distribution of the hitting probabilities $p_{k,\delta,g}$ at a given scale δ . Defining the scale-dependent multifractal exponents as

$$D_{q,\delta,g} = \frac{\ln \zeta(q, \delta, g)}{(q-1) \ln \delta},$$

one can obtain the multifractal exponents D_q by interpolation as $g \rightarrow \infty$ and $\delta \rightarrow 0$.

The efficiency of the GA FRW algorithm allowed us to simulate up to 10^{10} trajectories, while the generation order could be increased up to $g = 10$ in 2D, and $g = 7$ in 3D. It

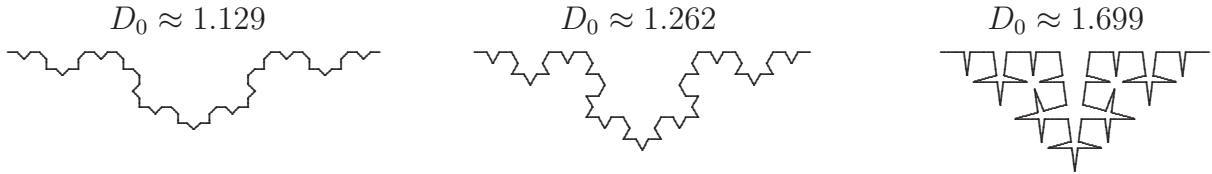


Figure 6: The third generation of three triangular von Koch curves.

is worth noting that these “limiting values” can be further extended by using parallel computation.

2.2.2 Interpolation of the scale-dependent exponents

First, we investigated the scale-dependent multifractal dimensions $D_{q,\delta,g}$ and its interpolation as the generation order g goes to infinity and the scale δ goes to 0. This is *a priori* a difficult problem because numerical simulations can only be realized for small generation orders and limited range of scales. We discovered and numerically checked the following interpolation formula [52]

$$D_{q,\delta_g,g} = D_q + c_q \frac{1}{g} + O(e^{-\alpha_q g}),$$

where the scale $\delta_g = (1/3)^g$ is chosen to be the smallest geometrical feature of the g -th generation, and c_q and α_q are parameters depending on q . This means that for a moderately large generation order g , $D_{q,\delta_g,g}$ is almost a linear function of $1/g$, up to exponentially small corrections. A linear regression of the values $D_{q,\delta_g,g}$ for several generation orders allows for a very accurate computation of the limiting values D_q of the multifractal dimensions. The accuracy of the whole computational method was verified by calculating the information dimension D_1 which is equal to 1 for any planar simply connected set (a result known as Makarov’s theorem) [57]. For the quadratic von Koch curve, we obtained $D_1 = 1.0000 \pm 0.0001$, such a precision being classified as very high for this kind of numerical computation.

2.2.3 Harmonic measure in 3D

The second important result of [52] is the numerical computation of the multifractal dimensions for the cubic von Koch surface of fractal dimension $D_0 = \ln 13 / \ln 3$. For the first time, the information dimension D_1 of a fractal surface was accurately calculated. Contrarily to an intuitive (but false) extension of the Makarov’s theorem in three dimensions, we obtained $D_1 = 2.007 \pm 0.002$, providing a concrete numerical counter-example to such an extension. It is worth noting that the first mathematical counter-example, for which D_1 was rigorously shown to be strictly greater than 2, was given in [58], but without providing the value of D_1 . Given that the obtained value 2.007 is very close to 2 for the cubic von Koch surface, one may wonder whether may exist or not irregular surfaces for which the excess $D_1 - 2$ is relatively large. Such surfaces would be particularly promising for designing efficient exchangers for diffusion-limited transport.

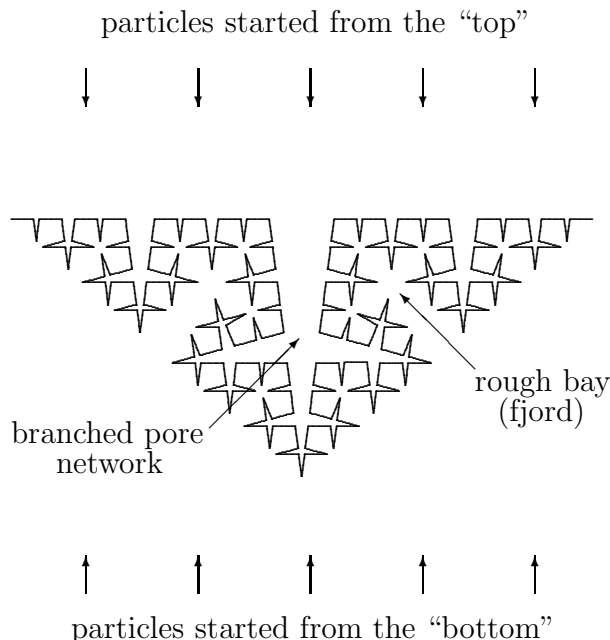


Figure 7: Fourth generation of the self-similar triangular von Koch curve with Hausdorff dimension $D_0 \simeq 1.699$. Depending on the side exposed to diffusing particles, this curve allows one to model either branched pore networks (source at the “top”) or fjord-like rough bays (source at the “bottom”).

2.2.4 What makes a boundary less accessible?

Although the scaling properties of the harmonic measure were largely studied, the relation between the geometry itself and its multifractal dimensions is still obscure. Is a more irregular boundary (greater fractal dimension D_0) more screened? How does the presence of deep fjords or a pore network modify the surface accessibility? More generally, what makes a boundary less accessible? This last question, which is closely related to different optimization problems in chemical engineering, has been addressed in [59]. By implementing the GA FRW algorithm, we calculated the multifractal dimensions D_q for two families of self-similar triangular von Koch curves of variable fractal dimension D_0 (Fig. 6). Changing the angle α between two intermediate segments of the generator from π to 0, the fractal dimension D_0 of these curves can be varied continuously from 1 to 2:

$$D_0 = \frac{\ln 4}{\ln(2 + 2 \sin(\alpha/2))}.$$

Depending on the side which is exposed to diffusing particles, the shape of these curves is geometrically very different so that one can speak about two families. Starting from a distant source at the top of Fig. 7, the particles progressively penetrate into smaller and smaller pores of the material. Such curves (called “top-seen”) could mimic the geometry of a branched pore network. In contrast, the diffusing particles started at the bottom of Fig. 7 arrive onto a rough surface with a fjord-like pore structure. The curves of this family are called “bottom-seen”.

The first and quite surprising result is that the multifractal dimensions D_q (shown on Fig. 8) turn out to be almost identical for the “top-seen” and “bottom-seen” curves

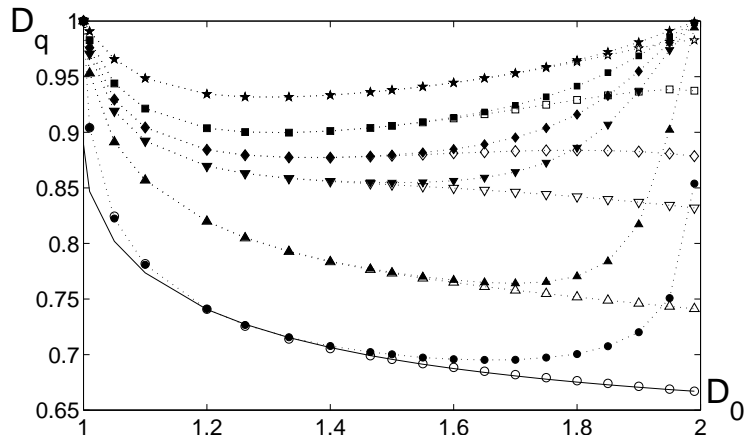


Figure 8: Positive-order multifractal dimensions D_q of the harmonic measure on the “top-seen” (solid symbols) and “bottom-seen” (open symbols) triangular von Koch curves of different fractal dimension D_0 : $q = 2$ (stars), $q = 3$ (squares), $q = 4$ (diamonds), $q = 5$ (up-pointing triangles), $q = 10$ (down-pointing triangles), and $q = \infty$ (circles). Dotted lines are a guide to the eye.

of the same fractal dimension when $D_0 \leq 1.3$. Being apparently different geometrically, these two types of morphologies are essentially indistinguishable for diffusing particles, i.e., when they are “seen” by the harmonic measure. At the same time, the spatial distributions of hitting probabilities $p_{k,\delta,g}$ over these two boundaries are very different. From a certain value of D_0 , the multifractal dimensions for the “top-seen” and “bottom-seen” curves split. In the former case, these dimensions approach 1, while in the latter case, they converge to smaller values. This behavior can be qualitatively explained by geometrical arguments (see [59] for details).

From this study, we draw attention to two facts. First, the fractal dimension D_0 , as a classical “measure” of the geometrical complexity, is not determinant for the diffusion screening: the harmonic measure on the “top-seen” curves with D_0 close to 2 exhibits almost the same scaling behavior as the harmonic measure on a smooth boundary since all the D_q are close to 1. This result provides a new insight into practical applications, e.g., in chemical engineering. Indeed, it shows that one does not need to explore very irregular shapes to diminish the multifractal dimensions. Second, the multifractal dimensions of the harmonic measure on the “top-seen” and “bottom-seen” curves are almost identical for moderate values of D_0 . This means that the harmonic measure is not sensitive to distinguish these boundaries of quite different geometry. The hierarchical self-similar structure of these curves is thus more determinant than their geometrical details.

2.3 Spread harmonic measures

The harmonic measure characterizes only the accessibility of a surface: how the particles reach the surface for the first time. When the surface is fully absorbing (infinite reaction or transfer rate W), the motion stops immediately after the first hit. When W is finite, the particle can be reflected from the surface to the bulk to resume its diffusion. In this case, the first arrival point and the final absorption (or reaction) point do not necessar-

ily coincide. It is the distribution of the absorption points that is really important for transport phenomena.

2.3.1 Effect of spreading and exploration length

At microscopic level, a finite transfer rate can be incorporated by introducing a sticking probability σ : once a particle reaches the boundary, it is either transferred (absorbed, relaxed, reacted, etc.) with probability σ , or reflected into the bulk with probability $1 - \sigma$ to resume its diffusive motion. For random walks on a lattice with mesh a , the sticking probability σ was related to the exploration length D/W as $\sigma = a/(a + D/W)$ [60]. The smaller the sticking probability, the larger the number of reflections that corresponds to “easy access, difficult transfer” situation (D/W is large). In this case, the particle has to explore a certain region of the surface around the first hitting point before being finally absorbed (or transferred). While the probability distribution of the arrival points is in general sharp and uneven due to diffusion screening, the distribution of the absorption points, at which the particles are transferred across the boundary, is getting smoother and spread by multiple reflections [61]. Figuratively speaking, reflections “fight” against diffusion screening and reduce its effect. In the ultimate case of fully reflecting boundary ($W = 0$ and $\sigma = 0$), each particle would explore the whole confining domain in an even manner, without diffusion screening at all.

The exploration length D/W controls the spreading effect: larger the D/W , further the particles spread around the first hitting point until their absorption. For a flat boundary (straight line in 2D or plane in 3D), we showed that approximately half of particles are absorbed by the disk of radius D/W around the first hitting point [62]. The exploration length D/W is thus a physical yardstick for quantifying the geometry.

2.3.2 Scaling properties of the spread harmonic measures

For a smooth boundary, the “spread harmonic measure” is defined for any (Borel) subset of the boundary as the probability for absorption of the partially reflected Brownian motion on this subset. This is a family of measures which are naturally parameterized by the length D/W , ranging from the harmonic measure at $D/W = 0$ to the Lebesgue measure at $D/W = \infty$. Then we studied numerically the scaling properties of the spread harmonic measures on finite generations of the quadratic von Koch curve [63].

The GAFRW algorithm was well suited for simulating Brownian trajectories in the bulk. The new implemented feature was partial reflections from the boundary. When the particle arrives on the boundary, a random number is generated to decide whether the particle is absorbed or not. If not, the particle is reflected (jumped at some small fixed distance a from the boundary) to resume its diffusive motion. As the exploration length is typically much larger than a , the sticking probability is very small, leading to a large number of reflections. The efficiency and rapidity of the GAFRW algorithm were therefore crucial for this study.

As in Sect. 2.2, the spread harmonic measures can be characterized by a set of multifractal exponents showing variations of the moments in Eq. (13) with the scale δ . The qualitative arguments for determining their scaling properties relied on comparison between several length scales: the smallest and largest geometrical lengths ℓ and L , the scale δ , and the exploration length D/W . Knowing for a straight line that the exploration

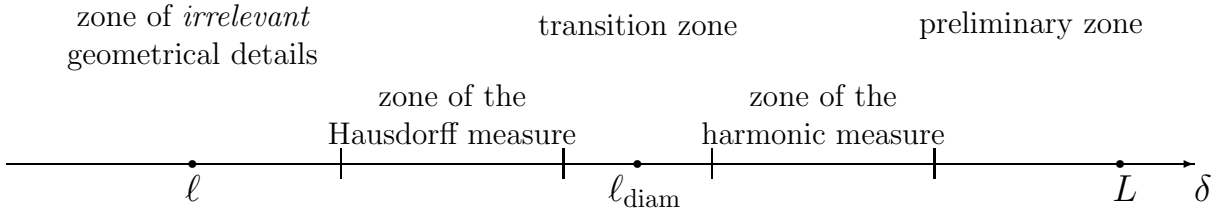


Figure 9: Schematic representation of scale zones of the spread harmonic measure. When δ is of order of the smallest geometrical detail ℓ , or smaller (on the left), one is looking at the harmonic measure of a linear segment. When δ is of order of the total size (diameter) L of the curve, or larger (on the right), the approximation of the spread harmonic measures is too coarse. The most interesting region $\ell \ll \delta \ll L$ includes the transition between the Hausdorff and harmonic measures.

length characterizes the region around the first hitting point where a half of particles are absorbed, we conjectured that, for irregular curves, D/W represents a perimeter of this region. For a fractal curve, the diameter of this region, ℓ_{diam} , is related to its perimeter by a scaling relation, $\ell_{\text{diam}} \sim \ell[(D/W)/\ell]^{1/D_0}$, D_0 being the fractal dimension and ℓ the smallest lengthscale of the boundary. The cases $\ell_{\text{diam}} \leq \ell$ and $\ell_{\text{diam}} \geq L$ trivially correspond to (almost) harmonic measure and (almost) Hausdorff measure (the Hausdorff measure is an extension of the classical Lebesgue measure to fractal objects, see [63] for details). The intermediate case with $\ell \ll \ell_{\text{diam}} \ll L$ is the most interesting. Depending on the ratio $\delta/\ell_{\text{diam}}$, the spread harmonic measures scale differently as schematically illustrated in Fig. 9. Figure 10 shows a continuous transition from the multifractal dimensions of the harmonic measure, D_q (studied in Sect. 2.2), to the multifractal dimension of the Hausdorff measure, D_0 . In addition, the developed concepts brought us to an alternative derivation of the anomalous constant phase angle (CPA) frequency behavior in electrochemistry [42, 64–67]. This new insight allowed us to explain some disagreements concerning the CPA exponent (see [63] for details).

From a mathematical perspective, a continuous transition between the harmonic and Hausdorff measures is a new interesting phenomenon. Although the presented study remained qualitative and relied on numerical analysis of prefractional curves, the observed results suggested a natural way for extending the spread harmonic measures to really fractal boundaries. The fact that a physical parameter D/W “tunes” the geometrical scale, at which the spread harmonic measures are looked at, may have potential applications. For instance, the diffusion screening, which is a fundamental obstacle in designing highly efficient exchangers, is progressively reduced by increasing the exploration length D/W . Moreover, the “functioning” of a system depends on the value of D/W . This means that such exchangers can be selective with respect to different species. For instance, this principle can potentially be used for designing a filter that would efficiently capture the species with a specific diffusion coefficient (i.e., specific size).

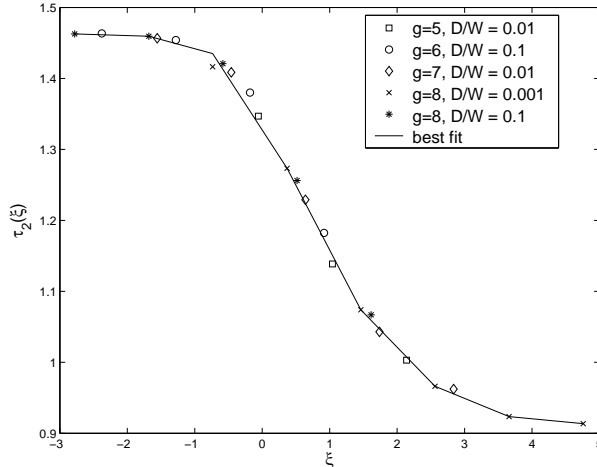


Figure 10: The scale-dependent multifractal dimension (with $q = 2$) of the spread harmonic measures on generations $g = 5, 6, 7, 8$ of the quadratic von Koch curve with different values of the exploration length D/W . All these dependencies, considered as functions of the scaling parameter $\xi = \ln(\delta/\ell_{\text{diam}})$, fall onto the same master curve $\tau_2(\xi)$. For small ξ or δ (on the left), one retrieves the multifractal dimension of the Hausdorff measure, which is equal to the fractal dimension of the curve, $D_0 = \ln 5 / \ln 3 \simeq 1.465$. For large ξ or δ (on the right), $\tau_2(\xi)$ approaches the correlation dimension of the harmonic measure, $D_2 \simeq 0.8925$ that we found in [52].

2.4 First passage statistics on fractal boundaries

Reflected Brownian motion is an intermittent process when diffusion steps in the bulk are altered by encounters with the surface. In the previous subsection, the active sites, which could absorb or transfer the diffusing particles, were supposed to be distributed uniformly over the boundary (spatially uniform sticking probability). In this case, the overall reaction process was shown to be realized in a region around the first hitting point and of the size of the exploration length. When, on the opposite, the active sites for reaction or transfer are diluted on the boundary, the surface is not homogeneously reactive any more. A more detailed study of individual diffusion steps in the bulk, known as Brownian excursions or bridges, is then needed [68].

2.4.1 First passage statistics

For a given boundary, we are interested in the two probability densities (Fig. 11):

- $\psi(t)$ that a particle, started from a close vicinity of the interface at $t = 0$, returns to this interface, for the first time, at time between t and $t + dt$;
- and $\theta(r)$ that the end-to-end Euclidean distance r between the starting and hitting points of the corresponding Brownian excursion (or bridge) lies between r and $r + dr$.

For flat surfaces, both densities are known explicitly. For instance, one has for a straight line in the plane [1]:

$$\psi(t) = \frac{a}{\sqrt{4\pi D} t^{3/2}} \exp[-a^2/(4Dt)], \quad \theta(r) = \frac{a}{\pi r^2},$$

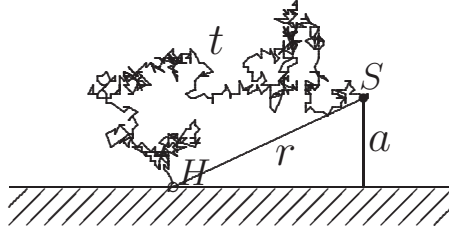


Figure 11: First passage statistics for a flat surface. Brownian motion started from a point S above the boundary (at distance a) hits this boundary at some (random) point H . The probability densities $\psi(t)$ and $\theta(r)$ describe the first hitting time t and the Euclidean end-to-end displacement r , respectively.

where a is the height of the starting point above the flat boundary (horizontal axis).² The asymptotic behavior of these densities at long time and large distance is described by power laws:

$$\psi(t) \propto t^{-\alpha} \quad (t \rightarrow \infty), \quad \theta(r) \propto r^{-\beta} \quad (r \rightarrow \infty), \quad (14)$$

with the exponents $\alpha = 3/2$ and $\beta = 2$. The first moment (average duration or displacement of an excursion) and the second moment of the former probability density functions are ill-defined and diverge mathematically speaking. But, in most practical situations, irregular interfaces are encountered and the behavior associated with flat interfaces is possibly misleading. It is thus important to know how an irregular geometry of the interface may affect the asymptotic behavior (14). In particular, what are the values of the exponents α and β for a fractal boundary? These issues had been addressed in [68].

2.4.2 Scaling relations

We first derive two general expressions describing the first-passage statistics of Brownian excursions (or bridges). A simple qualitative argument is the following. The total number $Q(t)$ of particles which have diffused out from the source is approximately proportional to the Minkowski content of the surface. The size of this content evolves in time as $t^{1/2}$, yielding $Q(t) \propto [t^{1/2}]^{d-D_0}$ for a boundary of fractal dimension D_0 , d being the dimension of the embedding space [69]. On the other hand, the total number $Q(t)$ is constituted of all the particles survived up to time t , $Q(t) \propto \int_0^t S(t') dt'$, while the survival probability $S(t)$ is related to the first hitting time density $\psi(t)$ as $S(t) = 1 - \int_0^t \psi(t') dt'$. Bringing

²It is important to stress that both densities depend on the parameter a . In particular, if a goes to 0, the densities $\psi(t)$ and $\theta(r)$ approach Dirac distribution $\delta(t)$ and $\delta(r)$, respectively. This reflects the well known fact that Brownian motion started from a smooth boundary crosses this boundary an infinite number of times during an infinitesimal time interval. In other words, Brownian motion immediately returns to the boundary. At first thought, this mathematical fact may sound as a puzzling paradox: Brownian motion simply cannot escape from the boundary.

From a physical of view, one should not forget that Brownian motion is a mathematical process which leads to the same macroscopic description as real microscopic dynamics (Sect. 1.1). In particular, the parameter a cannot be smaller than an interaction range between the surface and the diffusing particle (in the order of at least a few angstroms). What is important here is that the parameter a , whatever its physically limited value, is much smaller than the transport scales (variable r). In what follows, a will be considered as a given small parameter.

these together, one gets $\psi(t) \propto -d^2Q(t)/dt^2$ and

$$\alpha = \frac{D_0 - d + 4}{2}. \quad (15)$$

The displacement statistics $\theta(r)$ and the time statistics $\psi(t)$ are formally related according to

$$\theta(r) = \int dt \psi(t) \delta\left(\sqrt{\langle r^2(t) \rangle} - r\right),$$

where $\langle r^2(t) \rangle$ is the mean square displacement at time t . Assuming that the mean square displacement of the Brownian motion evolves as t in the bulk phase, a change of variable t for the delta distribution in the above equation gives, for a fractal boundary, $\theta(r) \propto 1/r^{2\alpha-1}$, and

$$\beta = 2\alpha - 1 \quad \Rightarrow \quad \beta = D_0 - d + 3. \quad (16)$$

The above qualitative arguments give an idea why and how the exponents α and β are related to the fractal dimension D_0 , without pretending for a mathematical rigor. A more rigorous derivation for the exponent β in 2D is sketched in [68].

2.4.3 Numerical verification

The scaling relations (15, 16) were checked by extensive numerical simulations for a class of self-similar and self-affine interfaces in two and three dimensions. In particular, diffusion near various triangular von Koch curves was simulated by the GAFRW algorithm. The starting points were chosen uniformly over a finite generation of the curve, within a small distance a . The simulation of a Brownian trajectory was terminated when the particle approached the boundary closer than a chosen threshold. For each particle, the duration and the end-to-end Euclidean displacement were recorded, providing large statistics for $\psi(t)$ and $\theta(r)$ (the number of simulated trajectories was 10^{10}). The data were fitted by power laws in order to determine the exponents α and β . The fact that the fractal dimension of the triangular von Koch curves can be continuously varied from 1 to 2 allowed us for a careful check of the scaling relations (15, 16). A good agreement between theoretical predictions and numerical results is shown in Fig. 12.

A simple dependence of α and β on the fractal dimension is a nontrivial result because diffusion screening and the harmonic measure properties might influence these exponents. The simulations confirmed that the Brownian dynamics in the bulk is not biased by a geometrical confinement induced by the boundaries. The exponent β is found to be strictly larger than 2. Consequently, the mean distance for the first-passage encounter is now finite in opposition with the case of a flat surface. The fact that Brownian bridges are sensitive to surface geometrical crossovers at long time should provide a way to probe colloidal shapes [70]. The studied first-passage process plays a central role in thermodynamics of rough colloidal surfaces [71], or in the evaluation of the mean first exit time from a bounded domain [72]. It is also important in nuclear magnetic relaxation in complex fluids and porous media [73].

2.5 Passivation processes

In the previous subsections, the surface activity remained constant in time. In practice, the boundary itself can be altered in the course of transport process. The passivation of

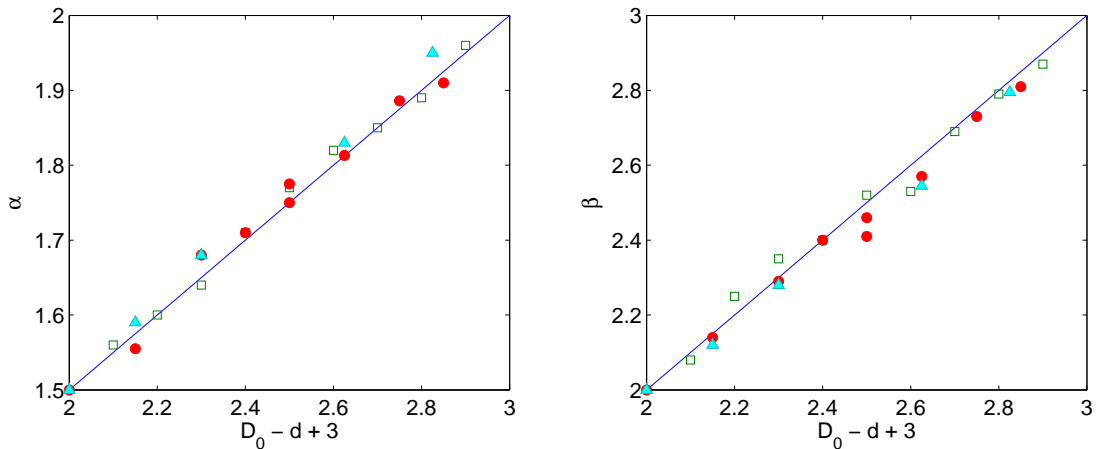


Figure 12: Variation of the exponent α (left) and β (right) with the boundary fractal dimension D_0 : self-similar curves in two dimensions (squares); self-similar surfaces in three dimensions (circles); self-affine surfaces in three dimensions (triangles). The solid line follows Eqs. (15) and (16), respectively.

the surfaces working under diffusion-limited conditions is a general phenomenon which appears in many natural or industrial systems ranging from catalysis [74] to heat transfer [75], electrochemistry [76], and physiology [38]. In such situations, it is not only diffusion screening which leads to a strongly inhomogeneous active surface, but part of the surface activity may be progressively inhibited by phenomena bearing different names, depending on the application field: passivation, fouling, poisoning or restricted absorption.

For instance, the transfer of nutrients from the digestive system to the blood in humans is mostly realized in the small intestine in which the major transport mechanisms are passive diffusion and absorption [77]. The anatomy of the small intestine exhibits a fractal-like geometry, with finger-like structures at many different scales of magnification: flexures, plicae, villi, microvilli [78]. In this type of geometry, the most exposed parts of the intestinal membrane are easily accessed by diffusion and thus are the first to be altered by any inflammatory disorder or any chemical species that would diffuse in the digestive system. As a matter of fact, a wide range of gastrointestinal disorders are associated with abnormal intestinal permeability [79].

Another important example of passivation is a parallel or serial “fouling” in heterogeneous catalysis [80]. During catalysis, this phenomenon consists in a parasitic reaction that passivates the catalyst in the regions which are active, and eventually eliminates the entire activity of these regions. Diffusion screening in irregular catalytic grains implies that active regions represent only a fraction of the total catalytic surface. The time evolution of the overall catalytic efficiency will then depend in a complex way on the accessibility of the more remote regions of the interface.

Finally, an enhanced efficiency of heat exchangers is often achieved by building interfaces of very large surface [81, 82]. But the functioning of these interfaces can be substantially altered by a fouling process, namely the scale deposition, in which crystalline deposits of low thermal conductivity locally reduce the heat transfer [83].

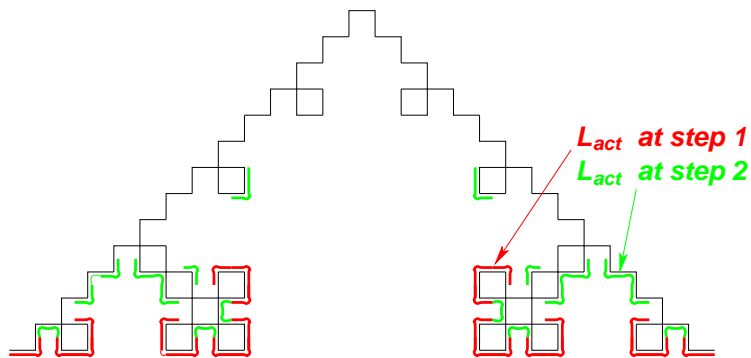


Figure 13: Schematic view of the successive active then passivated regions. The diffusing particles are coming from the bottom. The first active region is in red and has a length L_{act} . After the first step of the passivation process, the boundary condition on this region is set to Neumann, allowing a new region (in green) to become active. This region will be in turn passivated and so on, until the whole developed surface is passivated. In 2D, the active length L_{act} remains almost constant from one iteration to the next, until the entire surface is passivated.

2.5.1 Iterative passivation process

In this Section, we investigate the process of progressive passivation of irregular surfaces accessed by diffusion [84]. Passivation, disease, aging or fouling will likely start by damaging the most accessible part of the active interface, so the question then naturally arises: what happens after the initially active regions have been passivated? After deactivation, most of the diffusing particles hit a now passivated zone and are reflected, resuming their diffusion in the bulk to eventually react on an alive but deeper region of the catalytic surface (Fig. 13). Consequently, regions that were initially poorly active become fully active until they are in turn passivated. This passivation process goes on and on until, finally, the whole catalytic interface is deactivated and the catalytic process stops. The question of interest here is: how will the size of the region, where most of the particles finally react or are absorbed, evolve as the passivation process gradually deactivates the initial alive interface. In other words, how the activity is gradually transferred from the most accessible to less accessible regions.

In mathematical terms, the passivation process can be described as follows: at the beginning of the process, the alive sites are supposed to be uniformly distributed over the whole irregular surface. We suppose that the sticking probability σ is equal to 1 (or $W = \infty$) that corresponds to a homogeneous Dirichlet boundary condition on the concentration of reactant molecules. On such an interface, the activity, although existing in principle everywhere, is distributed in a very uneven manner due to diffusion screening. One may then define an “active zone” as the smallest part of the interface carrying a given (large) fraction p of the activity, e.g., 80%. The passivation process is then discretized and divided into the following steps [85]:

- At first, the entire interface is alive. The distribution of arrival probabilities at the interface is calculated by the GAFFRW algorithm on the quadratic and cubic von Koch boundaries as in Sect. 2.2.

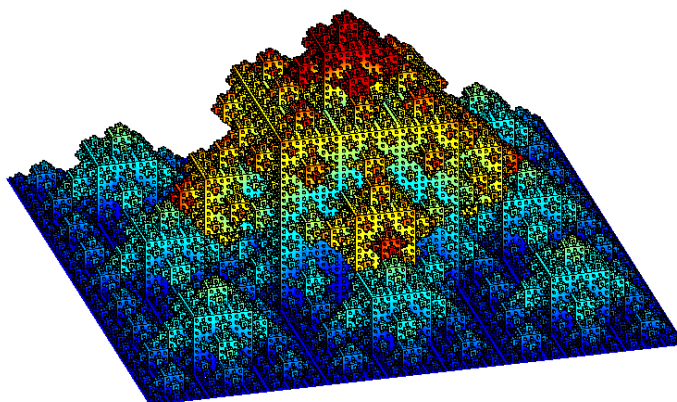


Figure 14: Successive active regions during the passivation process of a 5th generation of the cubic von Koch surface. Diffusing particles are coming from the bottom and reach first mainly the blue region of the interface. Each color in the simulation represents a set of 4 successive passivated regions (dark blue = regions 1 to 4, light blue = 5 to 8,...). One can see that the size of the active region decreases during the passivation process. At the end, only the dark red regions on the tip are active.

- The active region of the interface, which is only a fraction of the alive interface, is determined. The activity is proportional here to the harmonic measure density on the interface.
- This first active region is passivated. In mathematical terms, it would correspond to a particle concentration obeying Neumann boundary condition. Physically, it means that when a particle now hits a site belonging to this passivated region, it is reflected back and resumes its bulk diffusion until it reaches the regions that are still alive. In other words, this passivation process locally transforms a Dirichlet boundary condition into a Neumann boundary condition. The remaining alive interface thus consists in the former alive interface minus the newly passivated region.
- The new distribution of arrival probabilities is now computed using the new boundary condition (reflecting sites in the former active region).
- A new active region is determined, which is a subset of the remaining alive interface (the non passivated boundary). This new active region will be in turn passivated, and so on.

This passivation process generates at each iteration a new active region so that the whole interface can be decomposed as a sum of successive active regions.

2.5.2 Modification of the GAFRW algorithm

Although the GAFRW algorithm has proved to be very efficient, its direct application to a partially passivated boundary is still not sufficient to solve the problem here. The problem is the following: after a few iterations of the passivation process, the remaining

alive regions are highly screened. So a reactant particle launched from a distant source has to follow a very long stochastic trajectory, with a large number of reflections on the passivated sites of the boundary, before reaching any potentially active region. The extremely large computational time required for further passivation iterations makes then difficult or even impossible to study the whole passivation process. This difficulty was overcome by using the distribution of the activity at step n as the initial source distribution for the next step ($n + 1$). As a matter of fact, the distribution of the activity at step ($n + 1$) is composed of two types of particles: (i) particles arriving directly on the non passivated part of the boundary (corresponding to its contribution to the initial harmonic measure) and (ii) particles arriving after being reflected by the already passivated part of the boundary up to step n . The distant source of diffusing particles is thus replaced by a fictitious source on the boundary itself. Since the last passivated regions are close to the remaining alive zones, using them as sources considerably enhances the efficiency of the computation (see [84] for details).

This modification of the GAFRW algorithm has permitted us to study the passivation of the quadratic von Koch curve (2D) up to the 7th generation and of the cubic von Koch surface (3D) up to the 5th generation. One can take note visually of the complexity of the 3D surface and the evolution of the active zone in Fig. 14.

2.5.3 Comparison between 2D and 3D cases

In 2D, the active region has approximately a constant length L_{act} at each step of the process, as schematically indicated in Fig. 13. As one can see in Fig. 15 (left), this result is confirmed by numerical simulations for both the 4th and the 7th generations. The observed oscillations can be attributed to the discrete scaling of the deterministic interface. Moreover, it is known from previous studies that the size of the active region is of the order of the width of the interface [57, 85]. This implies that the number of passivation steps before the whole interface is deactivated should be of the order of the ratio between the total developed perimeter and the size of the interface. Quantitatively, the perimeter of the 4th generation (resp. 7th generation) of the quadratic Koch curve is $(5/3)^4 \approx 7.7$ times (resp. $(5/3)^7 \approx 35.7$ times) larger than the size of the system. Hence, one can see in Fig. 15 that the length of the active region becomes smaller than 50% of the width of the cell respectively after 8 and 37 passivation iterations. After that, in both cases the size of the active region falls rapidly.

In 3D, the striking result is that, unlike in 2D, the surface area of the active region S_{act} is not constant during the passivation process, but gradually decreases (as shown in Fig. 15(right) for $p = 80\%$). Even more, for the 5th generation, the developed surface in our 3D simulation contains $(13/9)^5 \approx 6.3$ times the projected surface, but 25 passivation iterations are necessary to completely passivate the surface. We can observe here a net discrepancy between the 2D and the 3D cases: due to the properties of Brownian motion, the passivation process is much steadier in 2D than in 3D, and it stops much more abruptly.

This observation is significant for the case of catalysis, where the need of a large surface within a finite volume implies the use of very irregular surfaces. As we have shown, the deep parts of the surface become more and more difficult to reach as the passivation gradually progresses, and the yield of reaction may decrease, despite the fact that active regions still exist. In other words, even when catalyst grains seem to be exhausted, they may still contain a large amount of alive surface. In this case, a large amount of catalyst

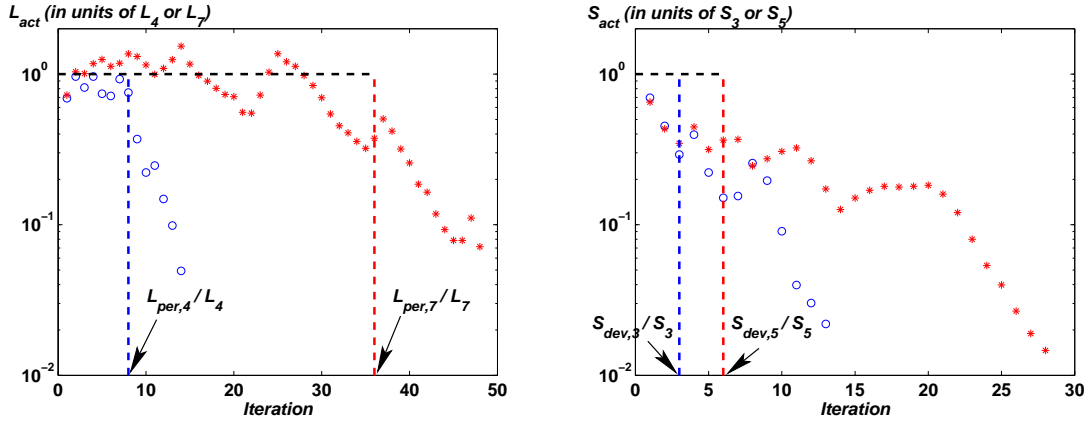


Figure 15: Comparison between passivation processes in 2D (left) and 3D (right). **Left.** The size L_{act} of the active region is plotted in units of the system width (L_4 and L_7 for generations 4 and 7 of the quadratic von Koch curve) at each step of the passivation process. Blue circles and red stars represent generations 4 and 7 in 2D (resp., 3 and 5 in 3D). One can see that the size L_{act} remains almost constant throughout the process, and is of the order of the structure width, until the number of iterations reaches the ratio between the perimeter of the interface and its width, L_{per}/L . These ratios are represented by the vertical dashed lines. After this threshold, the passivation process rapidly terminates. **Right.** The surface area S_{act} of the active region is plotted in units of the projected surface (S_3 and S_5 for generations 3 and 5 of the cubic von Koch surface) at each step of the passivation process. In contrast to the left plot, the active region at each step regularly decreases. It takes more than 25 steps to passivate the total surface at 5th generation, whereas the total developed surface represents only 6 times the projected surface. The vertical lines correspond to the ratio of the total developed surface ($S_{dev,3}$ and $S_{dev,5}$) on the projected surface (S_3 and S_5). Note the progressive slow decrease which is very different from the 2D case.

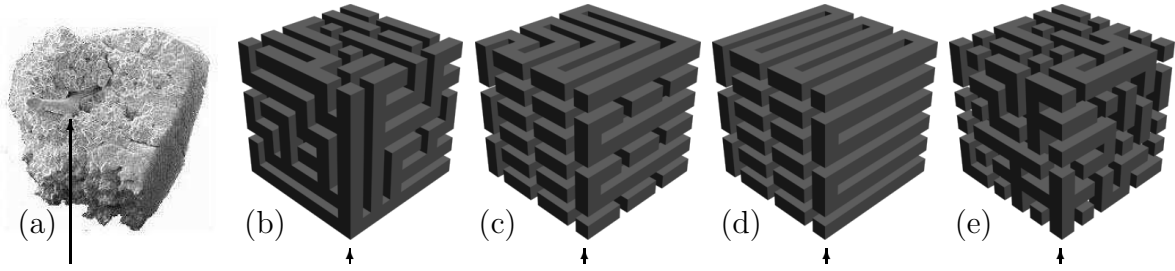


Figure 16: Five different geometrical structures with the same surface-to-volume ratio: (a) cast of a human acinus, (b) branched Kitaoka labyrinth, (c,d) two long channels “packed” in the cube, and (e) a disordered porous medium created by random “digging” in the cube. The first four domains satisfy the connectivity condition (accessibility from the “entry”, indicated by an arrow), while the last one does not. The “solid” channels represent the volume of the confining medium where a gas diffuses.

is wasted simply because the alive surface is not easily accessed by 3D diffusion anymore. From this point of view, an engineered (2+1)D geometry (with translational invariance) would be preferable.

2.6 Diffusion-weighted imaging of the lungs

The above studies were focused on various properties of the diffusive transport from a distant source towards an irregular boundary. In other words, we mainly considered what is the role of a geometrical irregularity of the interface. For this purpose, finite generations of self-similar von Koch boundaries were particularly suited. In many situations, however, the internal morphological, topological or geometrical structure of the confining domain appears to be even more significant. The examples are porous matrices of sedimentary rocks and sandstones, interstitial space of human skin, pulmonary acini, to name a few. Although the irregularity of the interface is still relevant, the structure of the whole diffusion-confining domain (e.g., pore size distribution, pore connectivity, etc.) may dominate the overall transport characteristics. In spite of the active research in this field, many questions still remain unanswered. This is probably because of a lack of reliable geometrical models that would be at the same time simple enough for performing numerical simulations and representative of porous media found in nature and industry. As an example, we refer to a recent progress in a quantitative understanding of the diffusive transport in the lungs [25, 86–88], which became possible thanks to the Kitaoka algorithm for generating a model geometry of the human pulmonary acinus [89].

2.6.1 The human pulmonary acinus and its modeling

A human pulmonary acinus, the gas exchange unit in the lungs, has a dichotomic branching structure with tortuous channels densely filling a given volume (Fig. 16a). A “Kitaoka acinus” is designed as a three-dimensional labyrinth of channels with square profile (Fig. 16b). Being well appropriate for numerical simulations, this simplified geometry captures the essential features of the pulmonary acinus: a dichotomic tree having non-symmetric branches of random lengths and filling a given volume. Moreover, the total surface area and the average length of the branches correspond to those of real acini.

We shall not discuss former works concerning oxygen diffusion in the lungs which were clarified by simulations in the Kitaoka acinus [25, 86–88]. In turn, we present Monte Carlo simulations that we developed to investigate restricted diffusion of hyperpolarized gases (like helium-3) and the consequent signal attenuation in a diffusion-weighted NMR experiment [90]. The aim of this study was to facilitate the development of a reliable MRI diagnosis of early stage emphysema which results in partial destruction of the alveolar tissue and enlargement of the distal airspaces. The geometry of emphysematous acini was modeled by removing randomly a fraction of the internal walls from previously generated Kitaoka labyrinth. We demonstrated that diffusion-weighted NMR could be sensitive to destruction of the branched structure. In fact, partial removal of the interalveolar tissue creates “loops” in the tree-like acinar architecture that enhance diffusive motion and the consequent signal attenuation.

2.6.2 Monte Carlo simulations accounting for magnetic field gradients

Given the specific shape of the Kitaoka acinus (long branched channels of the same square profile), there was no need for using fast random walks. An accurate accounting for a linear magnetic field gradient would further complicate an implementation of such an algorithm. For this reason, we limited ourselves to implementation of simple off-lattice random walks with normal reflections on the boundary of the Kitaoka acinus [90, 91]. The given temporal profile $f(t)$ of the applied magnetic field gradient was discretized on the simulation time interval $[0, t]$ with a time step $\tau = t/n$. The starting point \mathbf{r}_0 is chosen randomly with a uniform distribution inside the Kitaoka acinus. For each step k , one generates independent Gaussian displacements $d\mathbf{r}^i$ in the three space directions ($i = x, y, z$) with mean zero and dispersion $\sqrt{2D\tau}$, in order to pass from the current position \mathbf{r}_k to a new position \mathbf{r}_{k+1} . If the linear segment between the current position and the new position intersects the boundary, a mirror reflection is applied. At each step k , the term $\tau f(k\tau)\mathbf{r}_k^i$ is added to the phase counter φ_i for each space direction $i = x, y, z$. The total phase accumulated during the whole trajectory for unit gradient is then approximated, for each i , by the sum

$$\varphi_i = \tau \sum_{k=0}^n f(k\tau)\mathbf{r}_k^i.$$

If the gradient is applied along a given direction $\mathbf{e} = (e_x, e_y, e_z)$, the total phase accumulated in this direction for unit gradient is $\varphi_{\mathbf{e}} = e_x\varphi_x + e_y\varphi_y + e_z\varphi_z$. Although the gradient direction is fixed in the NMR scanner, the real acini in the lungs are oriented randomly. This effect is taken into account by looking at the signal that is averaged over all spatial directions. In this case, the averaged phase is $\varphi_{\text{av}} = \sqrt{\varphi_x^2 + \varphi_y^2 + \varphi_z^2}$. Repeating the Monte Carlo simulation N times, one records these phases in order to approximate their probability distribution. Once the simulations are terminated, one can find the signal E or the directionally averaged signal $S_{\text{av}}(g)$ as a function of the gradient amplitude g as

$$E \simeq \frac{1}{N} \sum_{j=1}^N \exp[i\gamma g \varphi_{\mathbf{e}}^j], \quad S_{\text{av}}(g) \simeq \frac{1}{N} \sum_{j=1}^N \frac{\sin(\gamma g \varphi_{\text{av}}^j)}{\gamma g \varphi_{\text{av}}^j}.$$

Since the statistical error of Monte Carlo technique is of order of $1/\sqrt{N}$, the choice of $N = 10^6$ leads to reasonably accurate results.

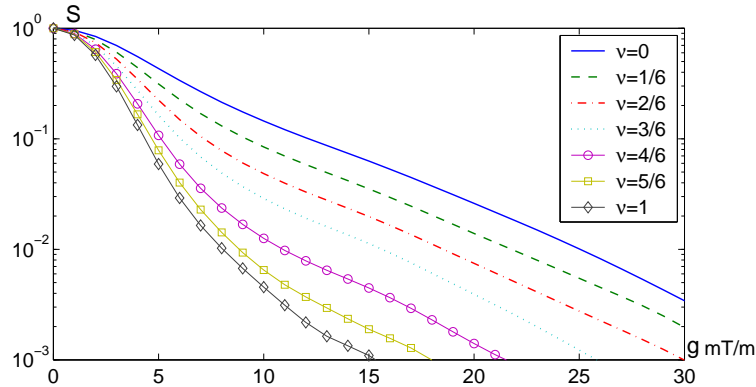


Figure 17: Directionally averaged signal $S_{av}(g)$ as a function of the gradient intensity g for different destruction factors ν starting from 0 (healthy acinus) and ranging up to 1 to model progressively damaged emphysematous acini. The signal is more attenuated in more damaged structures because diffusion is faster with a lower restriction. The ratio between the signals from a healthy acinus ($\nu = 0$) and that from an early emphysematous acinus ($\nu = 1/6$) is higher for larger gradient intensities.

2.6.3 Diffusion in healthy and emphysematous acini

Figure 17 illustrates the dependence of the directionally averaged signal $S_{av}(g)$ on the gradient intensity g for healthy and emphysematous acini. For weak gradient intensities, one recovers the classical (Gaussian) g^2 behavior of the logarithm of the signal, with a single apparent diffusion coefficient (ADC). Since partial destruction of the alveolar tissue by emphysema creates loops in the branched structure, diffusion becomes faster, and the signal is then more attenuated (larger ADC). The high sensitivity of diffusion-weighted NMR measurements to this effect can be potentially employed to diagnose emphysema at early stages.

The geometrical confinement and branching structure of the acinus lead to deviations from the g^2 behavior at higher gradients. In particular, one can see on Fig. 17 a transition to a stretched-exponential behavior known as localization regime [92, 93]. This observation indicates that the notion and use of ADC should be substantially revised, especially because experimental measurements at higher gradients appear to be more sensitive to the acinar structure. This also explains several confusions and possible ambiguities in determination of ADC in medical literature.

The numerical simulations were also performed on a tenfold scale Kitaoka acinus with a broad range of diffusion coefficients. The obtained results were confronted to experimental measurements in a tenfold phantom made from the standard epoxy resin by stereolithography [94, 95].

2.6.4 What is the role of a complex internal architecture?

In a separate work [96], we addressed a more general question: What is the role of a complex internal architecture (e.g., branching of the pulmonary acinus or pore network in rocks) for NMR measurements? To answer this question, we have performed Monte Carlo simulations of restricted diffusion in three groups of three-dimensional structures

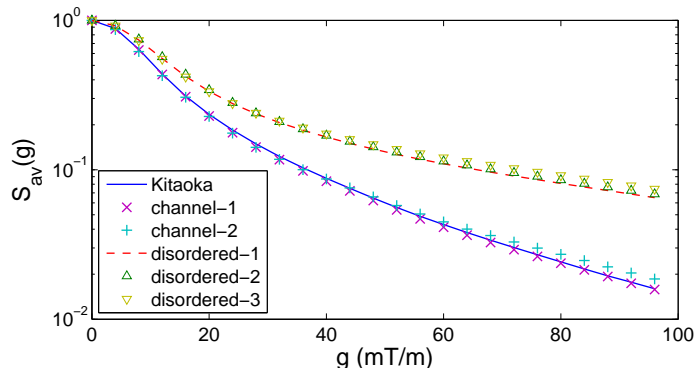


Figure 18: Directionally averaged signal $S_{av}(g)$ as a function of the gradient intensity g for different porous structures on Fig. 16 (the domains called “disordered-2” and “disordered-3” are not shown).

with the same surface-to-volume ratio. A basic domain is a cube of size L divided into $6 \times 6 \times 6 = 216$ small cubic cells. The first group is a set of random dichotomic labyrinths generated inside the cube by the Kitaoka algorithm (Fig. 16b). The second group consists of two realizations of a long channel filling the same cube (Fig. 16c,d). In the third group, disordered porous media are generated by connecting a number of randomly chosen adjacent cells (Fig. 16e). The directionally averaged signals from these structures are computed by the above Monte Carlo simulations. Figure 18 shows that the signal attenuation $S_{av}(g)$ for different branched structures (the first and second groups) are almost identical, while the signal for disordered media (the third group) is significantly higher. This is related to the fact that a disordered medium consists of a number of small disconnected patterns where the signal is less attenuated. The important conclusion is that the internal structure of porous media significantly influences the restricted diffusion and NMR measurements and should thus be taken into account for practical applications.

Summary

In this Section, we showed that Monte Carlo simulations were flexible and efficient tools for studying restricted diffusion in complex geometries, e.g., von Koch fractals. A geometry-adapted fast random walk algorithm allowed us to solve different problems, including multifractal properties of the harmonic measure in 2D and 3D (Sect. 2.2), scaling properties of the spread harmonic measures and the role of the exploration length (Sect. 2.3), first passage statistics (Sect. 2.4), passivation processes (Sect. 2.5), etc. All these problems concern restricted diffusion with different behaviors on the boundary. The GAFRW algorithm simulated Brownian trajectories in the bulk, while the boundary behavior was specifically implemented for each problem.

3 Spectral insight: Laplacian eigenfunctions

This section is devoted to the spectral description of restricted diffusion when the Laplace operator eigenfunctions allow one to structure the whole information about diffusion in a particularly useful form. Most diffusion characteristics (e.g., propagator, total flux, residence time, etc.) can be explicitly written in terms of the eigenfunctions. Specific features of these characteristics originate somehow from eigenfunctions. *We aim to reveal their relation and understand various features of restricted diffusion in complex geometries via the properties of the underlying Laplace operator eigenfunctions.* While this spectral description appears to be natural, it is not always considered as the most efficient way. In fact, except few simple domains, for which the Laplace operator eigenfunctions are known explicitly, a numerical calculation is required. This is a difficult time-consuming computational problem, especially for porous, multiscale, or irregular geometries. But, as far as the eigenfunctions are found for a given domain, the whole range of diffusion characteristics becomes directly accessible at once.

We used the spectral description as a unifying mathematical language for presenting the main achievements on restricted diffusion in NMR [14, 118, 119]. The diversity and complexity of diffusive NMR phenomena, observed in experiments, were shown to result from the specific properties of the reflected Brownian motion and the underlying Laplace operator eigenfunctions. Many classical results were retrieved, extended and critically discussed. In what follows, we present our main results basing on this spectral point of view.

3.1 Matrix formalism

Several matrix formalisms were developed for numerical analysis of the macroscopic signal formed by the nuclei diffusing in magnetic fields [27, 120–123]. We have reformulated and extended these formalisms to describe restricted diffusion in any geometrical confinement and arbitrary magnetic field [14, 124]. The “derivation” of the compact matrix form for the signal (shown in the next subsection) simply relies on a representation of the Bloch-Torrey equation (4) in the Laplace operator eigenbasis. The use of this natural basis allows one to get a *structured representation of diffusion* via two governing matrices Λ and \mathcal{B} . A truncation of these matrices for further numerical analysis is well controlled, leading to negligible computational errors. The use of the Laplace operator eigenfunctions is crucial here.

3.1.1 Perturbative derivation

When the applied magnetic field is independent of time, $B(\mathbf{r}, t) = \beta B(\mathbf{r})$, Eq. (4) reads as

$$\left(\frac{\partial}{\partial t} - D\Delta + i\gamma\beta B(\mathbf{r}) \right) c(\mathbf{r}, t) = 0, \quad (17)$$

where $B(\mathbf{r})$ is the normalized (dimensionless) spatial profile of an inhomogeneous magnetic field, and β its intensity. We are looking for a solution of this equation in the basis of the Laplace operator eigenfunctions $u_m(\mathbf{r})$ (of eigenvalues λ_m) satisfying Eqs. (9a, 9b):

$$c(\mathbf{r}, t) = \sum_{m'} \tilde{c}_{m'}(t) u_{m'}(\mathbf{r}), \quad (18)$$

with unknown time-dependent coefficients $\tilde{c}_{m'}(t)$. By construction, $c(\mathbf{r}, t)$ satisfies an appropriate boundary condition that was imposed for the eigenfunctions. Substitution of this expansion in Eq. (17), multiplication by $u_m^*(\mathbf{r})$, and integration over the confining domain Ω yield a set of ordinary differential equations on the coefficients $\tilde{c}_m(t)$

$$\frac{\partial \tilde{c}_m(t)}{\partial t} + \sum_{m'} \left(D\Lambda_{m,m'} + i\gamma\beta\mathcal{B}_{m,m'} \right) \tilde{c}_{m'}(t) = 0, \quad (19)$$

where the infinite-dimensional matrices Λ and \mathcal{B} represent the Laplace operator and the “perturbing” magnetic field $B(\mathbf{r})$ in the eigenbasis of the Laplace operator:

$$\mathcal{B}_{m,m'} = \int_{\Omega} d\mathbf{r} u_m^*(\mathbf{r}) B(\mathbf{r}) u_{m'}(\mathbf{r}), \quad (20)$$

$$\Lambda_{m,m'} = \delta_{m,m'} \lambda_m. \quad (21)$$

Thinking of $\tilde{c}_m(t)$ as components of an infinite-dimensional vector $C(t)$ leads to a matrix first-order differential equation

$$\left(\frac{d}{dt} + D\Lambda + i\gamma\beta\mathcal{B} \right) C(t) = 0. \quad (22)$$

As for a scalar equation, its solution is the (matrix) exponential:

$$\sqrt{V}C(t) = U e^{-(D\Lambda + i\gamma\beta\mathcal{B})t}. \quad (23)$$

The supplementary factor \sqrt{V} is put explicitly to get rid of the dimensional unit, meter^{-d/2}, of the vector $C(t)$ (V being the volume of the domain). Here the matrix exponential $e^{-(D\Lambda + i\gamma\beta\mathcal{B})t}$ acts on the left on the vector U representing the initial density $\rho(\mathbf{r})$ in the basis $\{u_m(\mathbf{r})\}$:

$$U_m = V^{1/2} \int_{\Omega} d\mathbf{r} u_m^*(\mathbf{r}) \rho(\mathbf{r}). \quad (24)$$

The macroscopic signal is then obtained according to Eq. (12) by integrating the transverse magnetization $c(\mathbf{r}, t)$ over the whole confining domain Ω with a sampling or pickup function $\tilde{\rho}(\mathbf{r})$ of the measuring coil or antenna:

$$E = \int_{\Omega} d\mathbf{r} c(\mathbf{r}, t) \tilde{\rho}(\mathbf{r}) = \sum_m \tilde{c}_m(t) \underbrace{V^{-1/2} \int_{\Omega} d\mathbf{r} u_m(\mathbf{r}) \tilde{\rho}(\mathbf{r})}_{\tilde{U}_m}. \quad (25)$$

The last sum can be interpreted as a scalar product between the vector $C(t)$ and the vector \tilde{U} representing the pickup function $\tilde{\rho}(\mathbf{r})$ in the basis of the eigenfunctions $\{u_m(\mathbf{r})\}$:

$$\tilde{U}_m = V^{-1/2} \int_{\Omega} d\mathbf{r} u_m(\mathbf{r}) \tilde{\rho}(\mathbf{r}). \quad (26)$$

The macroscopic signal at time t can thus be written in a compact matrix form of a scalar product:

$$E = \left(U e^{-(D\Lambda + i\gamma\beta\mathcal{B})t} \tilde{U} \right), \quad (27)$$

matrices being acting on the left. From a quantum-mechanical point of view, the matrix $e^{-(D\Lambda+i\gamma\beta\mathcal{B})t}$ can be thought of as an evolution operator acting on the initial state $\rho(\mathbf{r})$ (represented by the vector U), while the resulting density $c(\mathbf{r}, t)$ is weighted by the pickup or sampling function $\tilde{\rho}(\mathbf{r})$ (represented by vector \tilde{U}). A rapid increase of the eigenvalues λ_m with m allows one to truncate the matrices Λ and \mathcal{B} to moderate sizes in order to perform the numerical computation.

Although the compact matrix form (27) is derived for time-independent field $B(\mathbf{r})$, the approach is easily applicable to various NMR sequences. For instance, Carr-Purcell-Meiboom-Gill (CPMG) sequence consists in repeating the inverting 180° radio-frequency pulse n times to acquire successive echoes [125]. In the matrix formalism, the amplitude of the k th echo ($k = 1, \dots, n$) is simply calculated as

$$E_k = \left(U \left[e^{-(D\Lambda+i\gamma\beta\mathcal{B})t/(2n)} e^{-(D\Lambda-i\gamma\beta\mathcal{B})t/(2n)} \right]^k \tilde{U} \right).$$

We developed a spectral analysis of the multiple echo attenuation for CPMG sequences [126].

In general, one can approximate any given temporal profile $f(t)$ by a piecewise constant function: $f(t) = f_k$ on $[t_k, t_{k+1}]$ ($k = 0, \dots, K$). For each interval $[t_k, t_{k+1}]$, the Bloch-Torrey equation can be solved using the matrix exponential. In order to merge the solutions, the ending magnetization of the interval $[t_{k-1}, t_k]$ is taken as the initial condition for solving the problem on the next interval $[t_k, t_{k+1}]$. The use of the matrix representation is particularly efficient to handle such successive computations:

$$E = \left(U \left[\prod_{k=0}^K e^{-(D\Lambda+i\gamma\beta f_k \mathcal{B})(t_{k+1}-t_k)} \right] \tilde{U} \right), \quad (28)$$

where $t_0 = 0$ and $t_{K+1} = t$. It is worth stressing that this result is exact, no approximation was involved. Moreover, since any function can be approximated by a piecewise-constant function, the above relation allows one to *approximately* compute the signal for *arbitrary* temporal profile $f(t)$.

Conceptually, Eq. (27) is nothing more than a representation of the Bloch-Torrey equation in the Laplace operator eigenbasis. The matrices \mathcal{B} and Λ , depending merely on the eigenbasis and the spatial profile $B(\mathbf{r})$, have to be computed only once for a given geometry. Once this preliminary step is achieved, the computation of the signal for a given set of physical parameters is straightforward, accurate and very rapid. This is the crucial advantage with respect to conventional numerical techniques for solving the Bloch-Torrey equation (Monte Carlo simulations, finite difference or finite element methods, etc.).

As we pointed out in Sect. 1.4, the computational efficiency of the matrix formalism should not be surprising because finding the eigenbasis is equivalent to solving all the diffusive problems at once for a given geometry. Naturally, finding the eigenfunctions is a difficult task, especially for complex geometries. But once the eigenbasis is found, the remaining computations are easy. We are going to discuss the recent progress that we achieved by using the matrix formalism for simple geometries, for which the Laplace operator eigenbasis is known explicitly: a slab (an interval), a cylinder (a disk), and a sphere, as well as circular and spherical layers.

3.1.2 Moments

The compact matrix form (27) of the signal is particularly suitable for numerical purposes because the computation of matrix exponentials is rapid and very accurate. At the same time, a theoretical analysis with this form faces considerable difficulties because the governing matrices \mathcal{B} and Λ do not commute. In this subsection, we follow Ref. [14] and briefly discuss another strategy, when the signal is represented as a power series with the moments of the normalized total phase $\phi = \varphi/t$:

$$E = \mathbb{E}\{e^{iq\phi}\} = \sum_{n=0}^{\infty} \frac{(iq)^n}{n!} \mathbb{E}\{\phi^n\}, \quad (29)$$

where $q = \gamma\beta t$ is a dimensionless parameter characterizing the intensity of the applied field. Each moment can be explicitly written by using the definition (5) of ϕ :

$$\mathbb{E}\{\phi^n\} = \frac{n!}{t^n} \int_0^t dt_1 f(t_1) \int_{t_1}^t dt_2 f(t_2) \dots \int_{t_{n-1}}^t dt_n f(t_n) \mathbb{E}\{B(X_{t_1}) \dots B(X_{t_n})\}. \quad (30)$$

where the time moments t_1, \dots, t_n were put in ascending order. The multiple correlation function $\mathbb{E}\{B(X_{t_1}) \dots B(X_{t_n})\}$ can be calculated using the Markov property of Brownian motion:

$$\begin{aligned} \mathbb{E}\{B(X_{t_1}) \dots B(X_{t_n})\} &= \int_{\Omega} d\mathbf{r}_0 \rho(\mathbf{r}_0) \int_{\Omega} d\mathbf{r}_1 G_{t_1}(\mathbf{r}_0, \mathbf{r}_1) B(\mathbf{r}_1) \dots \\ &\int_{\Omega} d\mathbf{r}_n G_{t_n - t_{n-1}}(\mathbf{r}_{n-1}, \mathbf{r}_n) B(\mathbf{r}_n) \int_{\Omega} d\mathbf{r}_{n+1} G_{t - t_n}(\mathbf{r}_n, \mathbf{r}_{n+1}) \tilde{\rho}(\mathbf{r}_{n+1}). \end{aligned}$$

This lengthy expression has a simple probabilistic interpretation. Starting at time 0 from a randomly chosen point \mathbf{r}_0 (with a given initial density $\rho(\mathbf{r}_0)$), a particle diffuses up to time t_1 to point \mathbf{r}_1 where it “experiences” the magnetic field $B(\mathbf{r}_1)$. The diffusive propagator $G_{t_1}(\mathbf{r}_0, \mathbf{r}_1)$ describes this process. From \mathbf{r}_1 , the particle diffuses to a new point \mathbf{r}_2 , and so on. At last, the particle arrives at point \mathbf{r}_n at time t_n and experiences the magnetic field $B(\mathbf{r}_n)$. During the the remaining time $t - t_n$, the particle can diffuse to another \mathbf{r}_{n+1} where it is “sampled” with a given function $\tilde{\rho}(\mathbf{r}_{n+1})$. Using the spectral decomposition of the diffusive propagator $G_t(\mathbf{r}, \mathbf{r}')$, one can deduce a compact matrix form for the multiple correlation function [14]

$$\mathbb{E}\{B(X_{t_1}) \dots B(X_{t_n})\} = (U e^{-D\Lambda t_1} \mathcal{B} e^{-D\Lambda(t_2 - t_1)} \mathcal{B} \dots \mathcal{B} e^{-D\Lambda(t_n - t_{n-1})} \mathcal{B} e^{-D\Lambda(t - t_n)} \tilde{U}), \quad (31)$$

with the same matrices \mathcal{B} and Λ and vectors U and \tilde{U} as earlier. This is simply a representation of the above integral form in the Laplace operator eigenbasis.

In many practical cases, the boundary is purely reflecting (Neumann boundary condition), while the initial density $\rho(\mathbf{r})$ and sampling function $\tilde{\rho}(\mathbf{r})$ are uniform. It is easy to check that the components of the vectors U and \tilde{U} are then zero, except for the ground mode: $U_m = \tilde{U}_m = \delta_{m,0}$. Given that the matrices $e^{-D\Lambda t_1}$ and $e^{-D\Lambda(t - t_n)}$ are diagonal, the multiple correlation function reads as

$$\mathbb{E}\{B(X_{t_1}) \dots B(X_{t_n})\} = [\mathcal{B} e^{-D\Lambda(t_2 - t_1)} \mathcal{B} \dots \mathcal{B} e^{-D\Lambda(t_n - t_{n-1})} \mathcal{B}]_{0,0}.$$

For instance, the second moment is

$$\mathbb{E}\{\phi^2/2\} = \langle \sum_m \mathcal{B}_{0,m} e^{-D\lambda_m(t_2-t_1)} \mathcal{B}_{m,0} \rangle_2, \quad (32)$$

where $\langle \dots \rangle_2$ denotes the time integral in Eq. (30), for instance,

$$\langle e^{-D\lambda_m(t_2-t_1)} \rangle_2 = \frac{1}{t^2} \int_0^t dt_1 f(t_1) \int_{t_1}^t dt_2 f(t_2) e^{-D\lambda_m(t_2-t_1)}.$$

In this formal way, the original problem of finding the macroscopic signal of diffusing spins is entirely reduced to the analysis of the Laplace operator eigenmodes, and is thus solved as a physical problem. In what follows, we show how this mathematical basis can be applied for a theoretical analysis in many cases of particular interest.

3.2 NMR survey of restricted diffusion

In this section, we present various results on restricted diffusion in magnetic fields that we could obtain by using the Laplace operator eigenfunctions [14].

3.2.1 Simple geometries

Restricted diffusion in a slab (an interval), a cylinder (a disk), and a sphere is a classical problem [34, 35]. Since the Laplace operator eigenfunctions in these domains are known explicitly, many diffusion characteristics can be calculated analytically. For instance, the eigenfunctions and eigenvalues of the Laplace operator in the unit disk are

$$u_{nk}(\mathbf{r}) = \frac{\varepsilon_n}{\sqrt{\pi}} \frac{\beta_{nk}}{J_n(\alpha_{nk})} J_n(\alpha_{nk}r) \cos n\varphi, \quad \lambda_{nk} = \alpha_{nk}^2,$$

where $\varepsilon_n = \sqrt{2 - \delta_{n,0}}$, the constants $\beta_{nk} = \sqrt{\lambda_{nk}/(\lambda_{nk} - n^2 + h^2)}$ guarantee the normalization (10), $J_n(z)$ are the Bessel functions of the first kind, and α_{nk} are all the positive roots of the equations

$$zJ'_n(z) + hJ_n(z) = 0, \quad (33)$$

coming from the Robin boundary condition (9b), with $h = W/D$ ($L = 1$). The factorization of the dependences on the radial and angular coordinates r and φ is a direct consequence of the rotational invariance. It is worth stressing that here, the single index m is replaced by a double index nk (with $n = 0, 1, 2, 3, \dots$ and $k = 0, 1, 2, 3, \dots$) coming from enumeration of the positive roots α_{nk} . We shall use the double index as a convenient notation to enumerate the eigenvalues, eigenfunctions and the elements of matrices and vectors.

The explicit form of the eigenfunctions is employed to investigate the signal attenuation due to restricted diffusion in inhomogeneous magnetic fields (see [14] and references therein). This knowledge facilitates the construction of the matrix \mathcal{B} for a given profile $B(\mathbf{r})$. In general, this would require numerical integration in Eq. (20), but for some choices of the function $B(\mathbf{r})$, the integration can be realized analytically. In [14], we provided, for the first time, the explicit formulas for the matrix \mathcal{B} in two cases of practical interest:

a linear magnetic field gradient, $B(\mathbf{r}) = x$, corresponding to usual experimental setup for NMR measurements, and a parabolic magnetic field, $B(\mathbf{r}) = |\mathbf{r}|^2$. For example, we obtained for the unit disk in a linear gradient:

$$\mathcal{B}_{nk,n'k'} = \delta_{n,n'\pm 1}(1 + \delta_{n,0} + \delta_{n',0})^{1/2} \beta_{nk} \beta_{n'k'} \frac{\lambda_{nk} + \lambda_{n'k'} - 2nn' + 2h(h-1)}{(\lambda_{nk} - \lambda_{n'k'})^2}. \quad (34)$$

This matrix turned out to be fully expressed in terms of the eigenvalues λ_{nk} . This means that the originally complicated problem of computing the macroscopic signal attenuation is reduced to finding roots of the Bessel functions in Eq. (33). This result allows one for efficient numerical computation of the signal, as well as for a thorough theoretical analysis of the moments, as illustrated below.

3.2.2 Time-dependent diffusion coefficient

Apart from being a basis for efficient numerical computations, the matrix formalism is a powerful analytical tool. As a representative example, we consider a linear magnetic field gradient in a given direction \mathbf{e} and of intensity g :

$$\beta = gL, \quad B(\mathbf{r}) = (\mathbf{e} \cdot \mathbf{r})/L,$$

L being the characteristic size of the domain. For relatively small gradients (small q), the macroscopic signal in Eq. (29) is essentially determined by the second moment $\mathbb{E}\{\phi^2/2\}$:

$$E \simeq 1 - q^2 \mathbb{E}\{\phi^2/2\} + O(q^4) \simeq \exp[-q^2 \mathbb{E}\{\phi^2/2\}] + O(q^4) \quad (35)$$

(the first and other odd moments that would determine the phase of the signal are omitted). This formula known as ‘‘Gaussian phase approximation’’ (GPA) was widely employed in many theoretical, numerical and experimental studies of restricted diffusion (see [14] and references therein). It is worth noting that this formula becomes exact for free (unrestricted) diffusion, for which the second moment was calculated by Stejskal and Tanner for arbitrary temporal profile $f(t)$ of the applied gradient [127]

$$\mathbb{E}\{\phi^2/2\}_0 = \frac{D}{L^2} \langle (t_1 - t_2) \rangle_2. \quad (36)$$

Deviation of the second moment $\mathbb{E}\{\phi^2/2\}$ for restricted diffusion from its value $\mathbb{E}\{\phi^2/2\}_0$ for free diffusion can be used to characterize a confining domain. Actually, their ratio is directly related to apparent, effective or time-dependent diffusion coefficient $D(t)$ measured in NMR experiments³

$$D(t) = D \frac{\mathbb{E}\{\phi^2/2\}}{\mathbb{E}\{\phi^2/2\}_0}.$$

According to Eq. (35), this quantity is simply proportional to the logarithm of the macroscopic signal and is thus easily accessible in experiments. A number of studies related the behavior of the time-dependent diffusion coefficient and the geometry of a diffusion-confining domain [97].

³It is worth noting that this NMR definition of the time-dependent diffusion coefficient is different from its classical form, the latter being obviously independent of the applied magnetic field (see [14] for further discussion).

If there is no surface relaxation, Eq. (32) yields a general representation of the time-dependent diffusion coefficient for *any* confining domain and *arbitrary* temporal profile [14, 128]

$$\frac{D(t)}{D} = \sum_m L^2 \lambda_m \mathcal{B}_{0,m}^2 w_f(D\lambda_m t), \quad (37)$$

where the function $w_f(p)$ accounts for a given temporal profile $f(t)$:

$$w_f(p) = \frac{\langle e^{-p(t_2-t_1)/t} \rangle_2}{\langle -p(t_2-t_1)/t \rangle_2}. \quad (38)$$

It is easy to check the following normalization property for linear gradients (taking $L = 1$ for simplicity):

$$\sum_m \lambda_m \mathcal{B}_{0,m}^2 = 1$$

so that $\lambda_m \mathcal{B}_{0,m}^2$ can be considered as the weight of the m th eigenmode to the time-dependent diffusion coefficient. In turn, the eigenvalue λ_m determines a characteristic scale at which the contribution appears in Eq. (37) through the function $w_f(p)$. It is important to stress that Eq. (37) allows one to distinguish the roles of various “ingredients” of the problem. So, the spatial profile of the magnetic field enters only into the weights $\lambda_m \mathcal{B}_{0,m}^2$, while the temporal profile is fully taken into account by the function $w_f(p)$. Finally, the geometry determines both the time scales $(D\lambda_m)^{-1}$ and the weights $\lambda_m \mathcal{B}_{0,m}^2$. This connects directly the spectral properties of the Laplace operator to measurable characteristics of complex media.

The general representation (37) allowed us to retrieve and extend many classical results. In the long-time diffusion regime, when the diffusion length \sqrt{Dt} is much larger than L , the function $w_f(p)$ behaves as

$$w_f(p) \simeq p^{-2} \frac{\int_0^t dt f^2(t)}{\langle (t_1 - t_2) \rangle_2} + O(p^{-3}) \quad (p \gg 1), \quad (39)$$

yielding

$$E \simeq \exp \left[-\frac{\gamma^2 g^2 L^4}{D} \zeta_{-1} \int_0^t dt f^2(t) \right]$$

for any bounded domain, with the geometry-dependent dimensionless constant

$$\zeta_{-1} = \sum_m \mathcal{B}_{0,m}^2 (L^2 \lambda_m)^{-1}.$$

This is an extension of the classical results by Robertson and Neuman [129, 130]. It shows a high sensitivity of diffusion-weighted measurements to the size L of a confining domain in the long-time regime.

In the opposite short-time diffusion regime ($p \ll 1$), only a small fraction of particles near the boundary can “feel” their geometrical confinement, while the remaining majority of particles diffuse as they were in free (unbounded) space. The fraction of “restricted” particles can be estimated as the ratio between the volume of the diffusion layer of width \sqrt{Dt} near the boundary and the total volume: $S\sqrt{Dt}/V$, S being the total surface area.

The deviation of the time-dependent diffusion coefficient from its nominal (free diffusion) value D is then quantified by this ratio. A more rigorous analysis based on Eq. (37) gives [14]

$$\frac{D(t)}{D} \simeq 1 - \sqrt{Dt} \underbrace{\zeta_{3/2} \frac{S}{V}}_{\text{geometry}} \underbrace{\frac{\langle (t_2 - t_1)^{3/2} \rangle_2}{\langle (t_2 - t_1) \rangle_2 \sqrt{t}}}_{\text{temporal profile}} + O(t), \quad (40)$$

where $\zeta_{3/2}$ is a geometry-dependent constant. This is an extension of the classical result by Mitra *et al.* [131–133]. This relation was suggested for experimental measurement of the surface-to-volume ratio S/V in porous media.

3.2.3 Different diffusion regimes

In many cases of practical interest, the knowledge of the second moment is enough for an accurate approximation of the macroscopic signal. When the gradient intensity increases, the fourth and higher-order moments become progressively more and more significant (see also Sect. 3.2.5). In particular, Stoller and co-workers obtained the asymptotic behavior of the macroscopic signal at high gradient intensity for a slab geometry [92]:

$$E \propto \exp \left[-\frac{a_1}{2} (D\gamma^2 g^2 t^3)^{1/3} \right], \quad (41)$$

where $a_1 \simeq 1.0188$ is the absolute value of the first zero of the derivative of the Airy function. In this so-called localization regime, the signal is essentially formed by the nuclei diffusing (or “localized”) near the boundary and thus acquiring less dephasing than the nuclei in the bulk. Four years later, this theoretical prediction was experimentally confirmed by Hürlimann *et al.* [93]. Measuring the signal attenuation from water molecules diffusing between two parallel plates, Hürlimann and co-workers observed a spectacular deviation from the Gaussian g^2 dependence of $\ln E$ at gradient intensities higher than 15 mT/m.

In our review [14], we summarized different diffusion regimes (Fig. 19). Since diffusion and encoding in a spin-echo experiment can be set *independently*, we plot the signal as a function of the two dimensionless parameters $p = Dt/L^2$ and $q = \gamma g Lt$. From this plot, one can determine which kind of restricted diffusion is to be expected, and which formula should be applied to fit experimental data. It is worth noting, however, that this information is rather qualitative since the particular location of different regions on the diagram depends on the diffusion-confining geometry and applied magnetic field.

3.2.4 Rigorous results for relaxing boundaries

For three simple domains (interval, disk and sphere), many relevant quantities can be found analytically even in the presence of surface relaxation. Rigorous computations rely on explicit formulas for the elements of the matrices \mathcal{B} and Λ that were shown to be rational functions of the eigenvalues (e.g., Eq. (34)). Using the Laplace transform summation technique, we derived exact and explicit representations for the zeroth and second moments in the presence of surface relaxation [134]. Within the Gaussian phase approximation, these two moments determine the reference and diffusion-weighted signals, respectively.

Without presenting the details, we mention that the computation was essentially based on two observations:

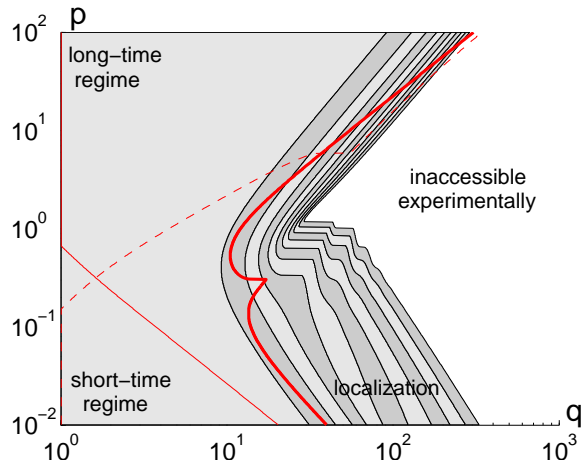


Figure 19: Different regimes of restricted diffusion in a slab under a linear magnetic field gradient. The signal is attenuated by a factor of 2 at each line separating two adjacent gray-scale regions (appearing as pale and dark stripes). The first large pale region on the left is composed of points (q, p) for which the signal E lies between $1/2$ and 1 . The next dark stripe regroups points (q, p) for which $1/4 \leq E \leq 1/2$, and so on. The white area on the right corresponds to pairs (q, p) for which the signal is below 10^{-3} . Since such a small signal is often comparable to noise, this area is referred to as inaccessible experimentally. On this pq diagram, the bold line delimits the region on the left in which the GPA predictions of the signal attenuation are valid with an accuracy of at least 5%.

- The Laplace transform of the even-order moments can be reduced to a combination of multiple sums of the form

$$\sum_{m_1, \dots, m_n} \frac{1}{(s_1 - \lambda_{m_1})^{\beta_1}} \frac{1}{(\lambda_{m_1} - \lambda_{m_2})^{\beta_{12}}} \frac{1}{(s_2 - \lambda_{m_2})^{\beta_2}} \frac{1}{(\lambda_{m_2} - \lambda_{m_3})^{\beta_{23}}} \cdots \frac{1}{(s_n - \lambda_{m_n})^{\beta_n}}$$

where $\{s_k\}$ is a set of real parameters, and $\{\beta_k\}$ is a set of positive integer numbers.

- Algebraic transformations and differentiations can reduce any sum of this form to the function

$$\sum_m \frac{1}{s - \lambda_m} \quad (42)$$

which can be calculated explicitly for the eigenvalues λ_m of the Laplace operator in the interval, disk, or sphere.

As a consequence, the Laplace transform of the even-order moments have explicit, though cumbersome, analytical forms. In particular, these explicit forms allow one to study the asymptotic behavior of the moments in different diffusion regimes. In the short-time regime, the series expansion in half-integer powers of the diffusion coefficient was generalized to arbitrary temporal profile of a linear magnetic field gradient. In the long-time regime, it was shown how the presence of surface relaxation modified classical Robertson's results (for details, see [134]).

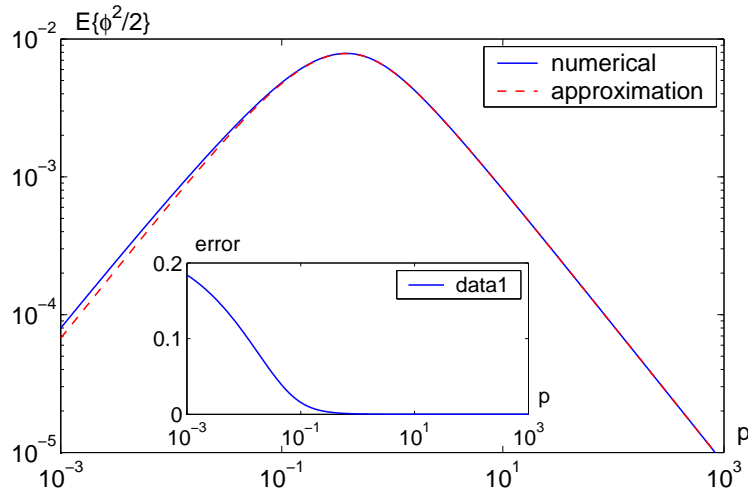


Figure 20: Numerically computed second moment $\mathbb{E}\{\phi^2/2\}$ for a linear gradient with bipolar temporal profile as a function of $p = Dt/L^2$ and its explicit approximation derived from the exact solution (43) for a cosine spatial profile. The inset shows relative deviation between them.

3.2.5 Cosine magnetic field in a slab

Although the above analysis could in principle be carried out for any even-order moment, its practical implementation was already tedious even for the second moment.

But a better knowledge of the high-order moments $\mathbb{E}\{\phi^n\}$ would help to understand the limits of applicability of the Gaussian phase approximation and the transition towards non-Gaussian regimes. We addressed this problem for restricted diffusion between parallel planes in a cosine magnetic field [135]. The specific choice of the spatial profile to be proportional to an eigenfunction of the Laplace operator in this confining geometry considerably simplified the underlying mathematics. In fact, the eigenfunctions of the Laplace operator on the unit interval ($L = 1$) with reflecting endpoints are simply $u_m(x) = \epsilon_m \cos(\pi m x)$, so that the substitution of the spatial profile $B(x) = \cos(\pi x)$ into Eq. (20) yields a particularly simple form

$$\mathcal{B}_{m,m'} = \frac{1}{\epsilon_m \epsilon_{m'}} (\delta_{m',m-1} + \delta_{m',m+1}),$$

where $\epsilon_m = \sqrt{2 - \delta_{m,0}}$ are the normalization constants. This subdiagonal structure of the matrix \mathcal{B} suggests the use of an analogy with reflected random walks to calculate the multiple correlation functions $\mathbb{E}\{B(X_{t_1}) \dots B(X_{t_n})\}$. For instance, the second moment with the cosine magnetic field is simply

$$\mathbb{E}\{\phi^2/2\} = \frac{1}{2} \langle \exp[-D\pi^2(t_2 - t_1)] \rangle_2. \quad (43)$$

Exact and explicit relations for several higher-order moments were also reported [135].

These results helped us to study the general structure and the properties of the high-order moments, as well as deviations from the GPA at magnetic fields of moderate or high intensity. Although the cosine magnetic field is indeed very specific (e.g., its experimental

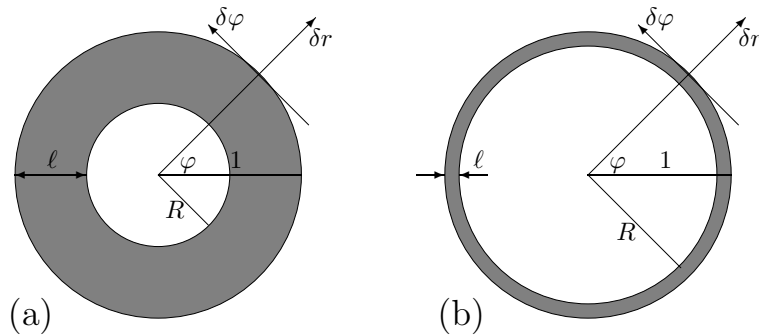


Figure 21: Circular layers of thickness $\ell = 1 - R$ with inner radius R and outer radius $L = 1$: $R = 0.5$ (a) and $R = 0.9$ (b). Note that variations in radial and angular coordinates are orthogonal to each other.

realization presents a challenge in itself), the deduced properties of the high-order moments provide a better understanding of the GPA and its limitations in general. Moreover, numerical simulations showed that the explicit relations obtained for the cosine magnetic field can be used as good approximations for linear magnetic field gradients (as illustrated in Fig. 20 for the second moment). Note also that Zielinski and Sen considered the cosine spatial profile to model and study susceptibility-induced local magnetic fields [136].

3.2.6 Diffusion in circular and spherical layers

There still exists a substantial “gap” in understanding restricted diffusion in simple geometries, on the one hand, and in natural porous media such as sedimentary rocks, cement, or biological tissues, on the other hand. From a theoretical point of view, the complexity of porous structures is related to multiple length scales, ranging from the size of tiny pores (in the order of several microns in some rocks) to the overall size of the sample (e.g., few centimeters). Moreover, porous media often present a hierarchical structure of pores so that intermediate characteristic length scales emerge. In this case, even the introduction of representative dimensionless parameters such as p , q , and h becomes ambiguous as being depended on a geometrical length L used. It is thus important to understand how classical theories for single-scale shapes (like a slab) can be extended to incorporate multiple scales. Since an analytical calculation in natural porous media is practically infeasible, some simplified confining domains with two or multiple length scales become particularly useful.

In this light, circular and spherical layers (or shells) appear as appropriate models (Fig. 21). Like for a disk and a sphere, the Laplace operator eigenbasis in these domains is known explicitly. Using the properties of the underlying Bessel equation, we derived explicit analytical formulas for the matrix \mathcal{B} representing a linear magnetic-field gradient (or parabolic magnetic field as well) in the Laplace operator eigenbasis [128]. From the numerical point of view, the problem is completely reduced to finding roots of the equations with Bessel functions. Once these roots are found, the governing matrices \mathcal{B} and Λ can easily be constructed and used to compute the macroscopic signal for any temporal profile of the magnetic field.

Bearing in mind multiscale structures, we particularly focus on thin layers (Fig. 21b),

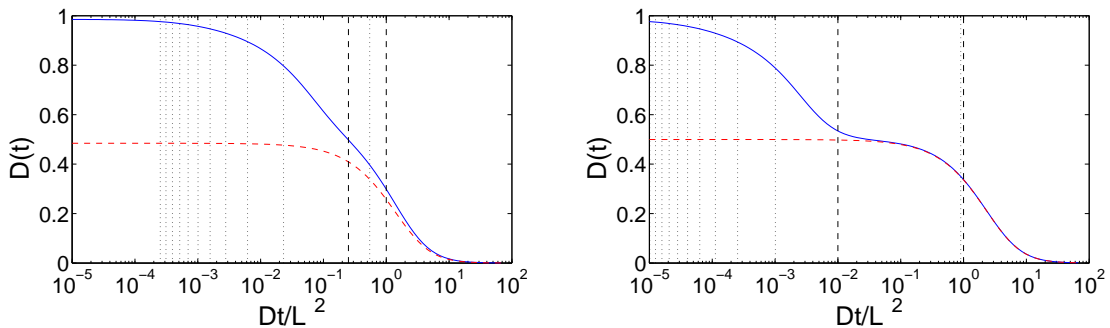


Figure 22: Normalized time-dependent diffusion coefficient $D(t)/D$ as a function of the dimensionless parameter $p = Dt/L^2$ ($L = 1$) for circular layers with inner radii $R = 0.5$ (left) and $R = 0.9$ (right). The solid line shows the exact computation via Eq. (44), while the dashed line represents an approximate solution containing only the first contributing eigenvalue λ_{10} and thus failing for small t . Two vertical dashed lines (at ℓ^2 and 1) roughly split the p axis in three regions: short-time regime (on the left, $p \ll \ell^2$), intermediate region, and long-time regime (on the right, $p \gg 1$). The vertical dotted lines show the scales λ_{1k}^{-1} (k ranging from 0 to 10, with $k = 0$ on the right and $k = 10$ on the left). One can observe a plateau due to a large separation between the two contributing eigenvalues λ_{10} and λ_{11} (the thinner the layer, the wider the plateau). Note that 2D diffusion in a thick circular layer (a 2D shape) is reduced to essentially one-dimensional motion in a thin circular layer, yielding the reduction factor $1/2$ (the level of the plateau).

for which perturbative calculations turned out to be surprisingly accurate (here we assume that there is no surface relaxation). For instance, the perturbation series of the eigenvalues in powers of the small dimensionless thickness ℓ are (in 2D):

$$\lambda_{n0} = n^2 \left(1 + \ell + \frac{5}{6}\ell^2 + \frac{2}{3}\ell^3 - \frac{n^2 - 16}{30}\ell^4 + O(\ell^5) \right),$$

$$\lambda_{nk} = \frac{\pi^2 k^2}{\ell^2} \left(1 + \frac{n^2 + 3/4}{\pi^2 k^2} \ell^2 + O(\ell^3) \right) \quad (k > 0),$$

so that the analysis is indeed much simpler for thin layers than for the unit disk (we took $L = 1$ so that the eigenvalues are dimensionless). The smallness of the thickness ℓ with respect to the perimeter 2π results in a large gap between $\lambda_{n0} \approx n^2$ and $\lambda_{nk} \approx \pi^2 k^2 / \ell^2$ with $k > 0$. The smaller eigenvalues $\{\lambda_{n0}\}$ describe large displacements in angular coordinates along the boundaries (i.e., along the circumference of the circular layer). In turn, the larger eigenvalues $\{\lambda_{nk}\}$ (with $k > 0$) describe small displacements in radial coordinate between the inner and outer boundaries. This situation is somehow analogous to restricted diffusion in a thin rectangle with sides π and ℓ , for which $\lambda_{nk}^{\text{rect}} = n^2 + \pi^2 k^2 / \ell^2$.

Apart from the above perturbative analysis and derivation of the explicit formulas for the matrix \mathcal{B} , the main result of [128] concerned the behavior of the time-dependent diffusion coefficient in these two-scale domains. Although the summation in Eq. (37) was carried out over all eigenmodes (here enumerated by double index nk), the rotation invariance of the circular and spherical layers eliminates the contributions of all eigenmodes

except for $n = 1$:

$$\frac{D(t)}{D} = \lambda_{10} \mathcal{B}_{10}^2 w_f(D\lambda_{10}t) + \sum_{k=1}^{\infty} \lambda_{1k} \mathcal{B}_{1k}^2 w_f(D\lambda_{1k}t). \quad (44)$$

In this sum, the first term with small eigenvalue $\lambda_{10} \approx 1$ (in 2D) is explicitly separated from the remaining terms with large eigenvalues $\lambda_{1k} \approx \pi^2 k^2 / \ell^2$. As we mentioned in Sect. 3.2.2, the function $w_f(p)$ slowly approaches 1 as p goes to 0, and has a power law decay (39) for p going to infinity. A large gap between λ_{10} and λ_{11} creates a region of values p such that $\lambda_{11}^{-1} \ll p \ll \lambda_{10}^{-1}$, for which the first term in Eq. (44) is nearly constant, while the other terms can be neglected. This suggests an emergence of an intermediate diffusion regime with a nearly constant $D(t)$, which is analogous to the tortuosity regime in porous media [97, 137]. This is a new, two-scale feature which could not be observed for one-scale domains such as the unit disk or sphere (Fig. 22). A complete analytical description developed in [128] allows one to study first the transition from the short-time diffusion to the intermediate (or tortuosity) regime at p around ℓ^2 , and then the transition to the ultimate long-time regime when p exceeds 1.

In general, the emergence of an intermediate region with a constant $D(t)$ would be a sign of a multi-scale geometry. Inversely, a significant separation in length scales in statistically homogeneous and isotropic porous media is expected to result in distinct constant regions in the behavior of $D(t)$. Since these regions can in principle be observed by varying the diffusion time t , this observation suggests an experimental way for detecting multiple scales. However, a reliable interpretation of such measurements still requires a substantial study of the Laplace operator eigenbasis in porous structures.

3.3 Residence times of reflected Brownian motion

In the previous subsection, we focused on NMR-oriented applications, when the choice of the “observable” $B(\mathbf{r})$ of Brownian motion to be a linear function of \mathbf{r} was dictated by a widespread use of a linear magnetic field gradient in modern NMR scanners. The range of problems that can be tackled by matrix formalism is much broader. We consider here another important choice for the “observable”, when $B(\mathbf{r})$ is equal to the indicator function $\mathbb{I}_A(\mathbf{r})$ of a subset A of the confining domain: $\mathbb{I}_A(\mathbf{r}) = 1$ for $\mathbf{r} \in A$, and 0 otherwise (Fig. 23). In this case, the random variable φ from Eq. (5) can be thought of as a “counter” which is turned on whenever the diffusing particles resides in A [138]. This is so-called residence or occupation time which is relevant for various diffusion-influenced reactions, for which the net outcome and the whole functioning of the system strongly depend on how long the diffusing particles remain in reactive zones (e.g., in a chemical reactor or biological cell) [139]. For instance, one can estimate the “trapping” time that particles spend in deep “fjord-like” pores of a catalyst. One can also mention surface relaxation processes in NMR [140] or kinetics of binding of ligands to a cell partially covered by receptors in microbiology [141].

The characteristic function $\mathbb{E}\{e^{iq\varphi}\}$ of the residence time φ is determined by Eq. (27), in which the matrix \mathcal{B} is defined according to Eq. (20) with $\mathcal{B}(\mathbf{r}) = \mathbb{I}_A(\mathbf{r})$:

$$\mathcal{B}_{m,m'} = \int_{\Omega} d\mathbf{r} u_m^*(\mathbf{r}) \mathbb{I}_A(\mathbf{r}) u_{m'}(\mathbf{r}) = \int_A d\mathbf{r} u_m^*(\mathbf{r}) u_{m'}(\mathbf{r}). \quad (45)$$

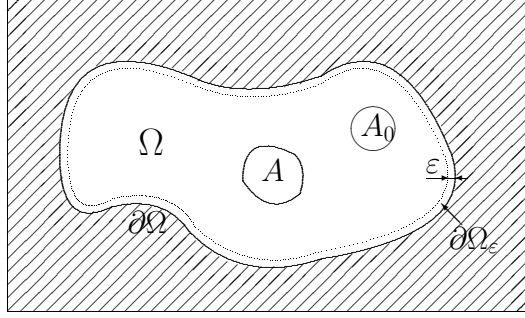


Figure 23: Diffusive motion of the particles restricted inside a bounded confining domain Ω with reflecting boundary $\partial\Omega$. The residence time φ indicates how long a diffusing particle, started somewhere in the domain (e.g., in the subset A_0), spends in a subset A until time t . The local time shows how long the particle spends in a close neighborhood (ε -vicinity or ε -sausage $\partial\Omega_\varepsilon$) of the boundary $\partial\Omega$.

The sampling function $\tilde{\rho}(\mathbf{r})$, determining the vector \tilde{U} , provides a way to weight or to condition the arrival points. In the simplest case with no conditioning, one uses $\tilde{\rho}(\mathbf{r}) = 1$. If one aims to investigate the survival probability of only those particles that arrive in some subregion Ω_0 of Ω , one takes $\tilde{\rho}(\mathbf{r}) \propto \mathbb{I}_{\Omega_0}(\mathbf{r})$ (Fig. 23).

With the matrix formalism, one can easily assess much finer and more detailed statistics of residence times. For instance, to compute the residence time of the diffusing particle between two times $0 < t_1 < t_2 < t$, a “counter” should be forced to turn on only during this period. Since the evolution of the system during two other periods $[0, t_1]$ and $[t_2, t]$ is unperturbed (no “counting” or “interaction”), Eq. (27) can be modified as

$$\mathbb{E}\{e^{iq\varphi}\} = (U e^{-D\Lambda t_1} e^{-(D\Lambda - iq\mathcal{B})(t_2 - t_1)} e^{-D\Lambda(t - t_2)} \tilde{U}).$$

Three matrix exponentials represent three successive time periods of the evolution. This “matrix product rule” can be applied in general, when one studies the residence time for a sequence of time intervals. Moreover, one can change the region of interest (set A) between different time periods in order to describe exchange processes between subsets (e.g., two pores of a medium).

We employed the matrix representation of Sect. 3.1.2 to investigate the long-time behavior of the moments of the residence time and to show that $\mathbb{E}\{\varphi^n\}$ is a polynomial of degree n as t goes to infinity [138]. The coefficients of this polynomial are expressed through the two governing matrices \mathcal{B} and Λ , and vectors U and \tilde{U} , using a diagrammatic representation. In addition, we considered cumulant moments $\prec \varphi^n \succ$ defined as coefficients of the series

$$\ln \mathbb{E}\{e^{iq\varphi}\} = \sum_{n=1}^{\infty} \frac{(iq)^n}{n!} \prec \varphi^n \succ.$$

We argued that all the cumulant moments behave as linear functions of t at long times:

$$\prec \varphi^n \succ \simeq b_{n,1}t + b_{n,0},$$

where the coefficients $b_{n,k}$ were explicitly given by using a diagrammatic representation. This statement was explicitly demonstrated for the cumulant moments up to the order

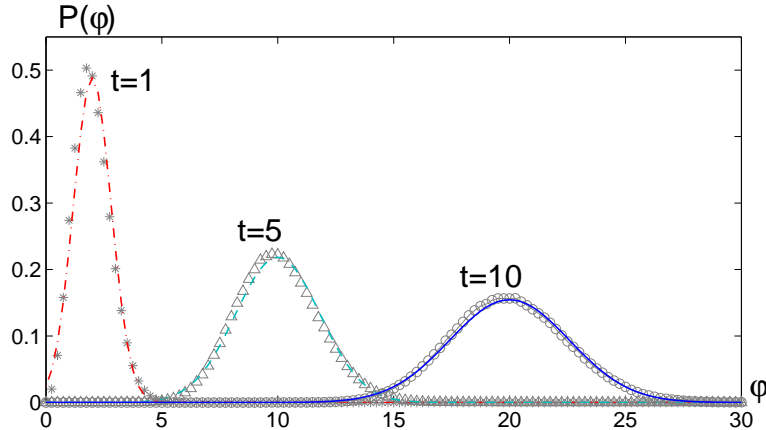


Figure 24: The probability distribution of the local time of reflected Brownian motion on the unit interval at times $t = 1, 5, 10$ (stars, triangles, and circles, respectively) obtained by Monte Carlo simulations, and its Gaussian approximation with mean $b_{1,1} = 2$ and variance $b_{2,1} = 2/3$ (dashed-dotted, dashed, and solid lines, respectively).

4 and checked numerically for several higher orders. Since the variance $\langle \varphi^2 \rangle$ linearly increase in time, it is natural to renormalize φ by \sqrt{t} . The first cumulant moment of the new random variable φ/\sqrt{t} is still increasing in time, while its variance approaches a constant. In contrast, higher-order cumulant moments with $n > 2$ go to 0. In the long-time limit, the probability distribution of the normalized random variable φ/\sqrt{t} becomes closer and closer to a Gaussian distribution with mean $b_{1,1}\sqrt{t}$ and variance $b_{2,1}$, where

$$b_{1,1} = \mathcal{B}_{0,0}, \quad b_{2,1} = 2 \sum_m \mathcal{B}_{0,m}^2 \lambda_m^{-1}.$$

As a consequence, the normalized residence time φ/\sqrt{t} is getting closer and closer to a Gaussian variable as time t grows. These theoretical results are successfully confronted with Monte Carlo simulations (Fig. 24).

3.3.1 Local time on the boundary

The definition of reflected Brownian motion in Sect. 1.3 involves the local time ℓ_t which characterizes the residence time on the boundary

$$\ell_t = \lim_{\varepsilon \rightarrow 0} \frac{1}{\varepsilon} \int_0^t ds \mathbb{I}_{\partial\Omega_\varepsilon}(X_s),$$

where $\partial\Omega_\varepsilon$ is the ε -vicinity of the boundary $\partial\Omega$: $\partial\Omega_\varepsilon = \{\mathbf{r} \in \Omega : |\mathbf{r} - \partial\Omega| \leq \varepsilon\}$ (Fig. 23). The local time ℓ_t is also related to the statistics of finite-distance reflections from the boundary, which is crucial for intermittent Brownian dynamics [70, 142–144]. The characteristic function of the local time is given by Eq. (27) with the matrix \mathcal{B} determined by substituting $B(\mathbf{r}) = \mathbb{I}_{\partial\Omega_\varepsilon}/\varepsilon$ in Eq. (45). When normalized by ε , the integral over the ε -vicinity $\partial\Omega_\varepsilon$ converges to the surface integral over the (smooth) boundary $\partial\Omega$, yielding

$$\tilde{\mathcal{B}}_{m,m'}^s = \int_{\partial\Omega} d\mathbf{r} u_m^*(\mathbf{r}) u_{m'}(\mathbf{r}). \quad (46)$$

Here, the passage to the limit $\varepsilon \rightarrow 0$, which is in general delicate and time-consuming for other numerical techniques is implemented intrinsically. This is one of the crucial advantages of the matrix formalism for computing local times.

3.3.2 Surface relaxation mechanism

The matrix formula (27) for the macroscopic signal exhibits the explicit dependence on the physical parameters D and $\gamma\beta$, characterizing respectively diffusion and encoding. In turn, the dependence on the surface relaxivity W remains implicit, as being incorporated via the Robin boundary condition (9b) for the eigenfunctions. As a consequence, the eigenfunctions, the eigenvalues, and the governing matrices Λ and \mathcal{B} have to be recalculated for each new value of the surface relaxivity W . Since their computation is in general the most time-consuming step, such an implicit dependence on W can be considered as a drawback of matrix formalisms.

This drawback can be overcome by introducing relaxation mechanisms via an inhomogeneous distribution of relaxation rates $\tilde{B}(\mathbf{r})$ in Eq. (4) with *Neumann boundary condition*. Surface relaxation can be implemented via a distribution $\tilde{B}(\mathbf{r})$ localized near the boundary, e.g., $\tilde{B}_\varepsilon(\mathbf{r}) = \varepsilon^{-1}\mathbb{I}_{\partial\Omega_\varepsilon}(\mathbf{r})$. In the limit ε going to 0, the volume integral in Eq. (20), determining the governing matrix \tilde{B} , is reduced to the boundary integral (46).

Since the mechanisms of gradient encoding and of bulk or surface relaxations are independent, their effects are simply superimposed as a linear combination of the corresponding terms in Eq. (4). Consequently, the above expressions for the signal can be easily modified to include different attenuation mechanisms. For instance, Eq. (27) for the FID in the presence of surface relaxation becomes

$$E = (U e^{-(D\Lambda + i\gamma\beta\mathcal{B} + W\tilde{\mathcal{B}}^s)t}\tilde{U}).$$

The advantage of this relation is the explicit dependence on all three physical parameters D , $\gamma\beta$, and W . The structure of each term has a clear physical interpretation: $D\Lambda$ describes restricted diffusion, $i\gamma\beta\mathcal{B}$ represents the dephasing, and $W\tilde{\mathcal{B}}^s$ accounts for surface relaxation. One can similarly extend other matrix formulas for the CPMG sequence or any temporal profile. Nonuniform bulk or surface relaxations can also be incorporated.

It is crucial to stress that here the eigenvalues and eigenfunctions are defined for Neumann boundary condition, whatever the value of surface relaxivity W is. As a consequence, these eigenfunctions, as well as the governing matrices Λ , \mathcal{B} , and $\tilde{\mathcal{B}}^s$, depend only on the diffusion-confining geometry and have to be constructed only once for a given confining domain. The introduction of the matrix $\tilde{\mathcal{B}}^s$ is therefore an alternative way to incorporate uniform surface relaxation. Moreover, it is a general frame for dealing with a nonuniform distribution $\tilde{B}(\mathbf{r})$ of the relaxation rates, either in the bulk, or on the boundary. This concept is easily extendable for a superposition of various attenuation mechanisms. For instance, one can study the combined effect of the surface and bulk relaxations, gradient encoding, presence of dipolar magnetic field, etc.

Conclusion

In this work, we presented theoretical and numerical results that we achieved in the course of the last five years. In order to study restricted diffusion in complex geometries, we combined probabilistic tools with spectral analysis.

An implementation of Monte Carlo techniques that we specifically adapted to several model geometries allowed us to shed a new light onto diffusion in complex media. With these tools, we tackled such problems as multifractal properties of the harmonic measure in 2D and 3D (Sect. 2.2), scaling properties of the spread harmonic measures and the role of the exploration length (Sect. 2.3), first passage statistics (Sect. 2.4), passivation processes (Sect. 2.5), diffusion-weighted imaging of the lungs (Sect. 2.6). These problems come from different fields (harmonic analysis, heterogeneous catalysis, heat transfer, nuclear magnetic resonance, physiology, medicine, etc.), in which geometrical complexity plays a central role.

Monte Carlo techniques successfully answer the question *how* particles diffuse in a given medium. However, they may fail to explain *why* some features of diffusion are common while others are too specific or geometry-dependent. In other words, what differentiates various confining media in respect of diffusion? This question is tightly related to inverse and optimization problems which consist in determining or designing geometry according to some diffusion characteristics. A spectral approach provides a unifying mathematical “language” for tackling these problems. In fact, many diffusion characteristics can be expressed in terms of the Laplace operator eigenfunctions whose properties are therefore a source of potentially important information. For instance, the interplay between these eigenfunctions and a linear magnetic field gradient yielded an intermediate diffusion regime for thin circular and spherical layers (Sect. 3.2.6). More generally, the spectral approach was successfully applied to retrieve, extend, and critically discuss various results on restricted diffusion in NMR (Sect. 3.2). Residence time and other functionals of reflected Brownian motion could as well be analyzed (Sect. 3.3). The investigation of restricted diffusion in complex geometries based on the study of the properties of the underlying Laplace operator eigenbasis is our principal guideline.

Many questions about diffusion in complex geometries remain open. On the one hand, a further study of restricted diffusion in model geometries (such as packs of spheres or cylinders) will reveal and help to better understand various features of this process. On the other hand, it is possible to apply the developed arsenal of theoretical and numerical methods to complex structures in nature and industry: a three-dimensional porous morphology of a cement paste reconstructed by X-ray microtomography; skin interstitial space; the human placenta; the lungs, to name a few. Although a complete comprehension of diffusion in natural geometries is unrealistic because of their complexity, this very complexity may help in averaging out specific features of the confining media and of transport processes. A practical goal of this study is to reveal relevant characteristics of the medium that would essentially determine and control diffusive transport.

Acknowledgments

A cross-disciplinary character of the presented works could not be maintained without collaborations. The presented results have been obtained together with J. S. Andrade, M. Filoche, G. Guillot, P. Levitz, B. Sapoval, and M. Zinsmeister. I'm grateful to B. Duplantier, T. Iakovleva, P. Levitz and M. Plapp for careful proofreading of the manuscript and numerous advices.

References

- [1] W. Feller, *An Introduction to Probability Theory and Its Applications*, Third ed. (New York: John Wiley, 1968).
- [2] M. Kac, “Can One Hear the Shape of a Drum?”, *Am. Math. Monthly* **73**, 1-23 (1966).
- [3] R. L. Liboff, *Kinetic Theory: Classical, Quantum, and Relativistic Descriptions*, 3rd Ed. (Springer-Verlag, New York, 2003).
- [4] E. M. Lifshitz and L. P. Pitaevskii, *Physical Kinetics*, Volume 10 of *Course of Theoretical Physics* (Pergamon International Library of Science, Technology, Engineering, and Social Studies, 1981).
- [5] J. Klafter and J. M. Drake (Eds.). *Molecular Dynamics in Restricted Geometries* (New York: John Wiley and Sons, 1989).
- [6] J.-P. Bouchaud and A. Georges, “Anomalous diffusion in disordered media: Statistical mechanisms, models and physical applications”, *Phys. Rep.* **195**, 127-293 (1990).
- [7] M. F. Shlesinger, J. Klafter, and G. Zumofen, “Above, below and beyond Brownian motion”, *Am. J. Phys.* **67**, 1253-1259 (1999).
- [8] R. Metzler and J. Klafter, “The random walk’s guide to anomalous diffusion: a fractional dynamics approach”, *Phys. Rep.* **339**, 1-77 (2000).
- [9] S. Havlin and D. ben Avraham, “Diffusion in disordered media”, *Adv. Phys.* **51**, 187-292 (2002).
- [10] R. Kimmich, “Strange kinetics, porous media, and NMR”, *Chem. Phys.* **284**, 253-285 (2002).
- [11] M. S. Birman and M. Z. Solomyak, *Spectral Theory of Self-Adjoint Operators in Hilbert Space* (D. Reidel Publishing Company, 1987).
- [12] B. D. Hughes, “Random Walks and Random Environments” (Clarendon Press, Oxford, 1995).
- [13] G. H. Weiss, *Aspects and Applications of the Random Walk* (North-Holland, Amsterdam, 1994).
- [14] D. S. Grebenkov, “NMR survey of reflected Brownian motion”, *Rev. Mod. Phys.* **79**, 1077-1137 (2007).
- [15] M. Kac, “On the distribution of certain Wiener functionals”, *Trans. Am. Math. Soc.* **65**, 1-13 (1949).
- [16] M. Kac, “On some connections between probability theory and differential and integral equations”, in “Proc. 2nd Berkeley Symp. Math. Stat. Prob.” edited by J. Neyman, pp. 189-215 (University of California Press, Berkeley, 1951).

- [17] M. Freidlin, *Functional Integration and Partial Differential Equations*, Annals of Mathematics Studies (Princeton University Press, Princeton, New Jersey, 1985).
- [18] B. Simon, *Functional integration and quantum physics* (Academic press, London, New York, San Francisco, 1979).
- [19] R. F. Bass, *Diffusions and Elliptic Operators* (Springer, New York, 1998).
- [20] K. K. Sabelfeld, *Monte Carlo Methods in Boundary Value Problems* (Springer-Verlag: New York - Heidelberg, Berlin, 1991).
- [21] K. K. Sabelfeld and N. A. Simonov, *Random Walks on Boundary for Solving PDEs* (Utrecht, The Netherlands, 1994).
- [22] G. N. Milshstein, *Numerical Integration of Stochastic Differential Equations* (Kluwer, Dordrecht, the Netherlands, 1995).
- [23] B. Sapoval, “General Formulation of Laplacian Transfer Across Irregular Surfaces”, *Phys. Rev. Lett.* **73**, 3314-3316 (1994).
- [24] B. Sapoval, “Transport Across Irregular Interfaces: Fractal Electrodes, Membranes and Catalysts”, in *Fractals and Disordered Systems*, Eds. A. Bunde, S. Havlin, 233-261 (Springer, 1996).
- [25] M. Felici, M. Filoche, C. Straus, T. Similowski, and B. Sapoval, “Diffusional screening in real 3D human acini - a theoretical study”, *Resp. Physiol. Neurobiol.* **145**, 279-293 (2005).
- [26] Yu. A. Makhnovskii, A. M. Berezhkovskii, and V. Yu. Zitserman, “The Trapping of Diffusing Particles by Absorbing Surface Centers”, *Russian J. Phys. Chem.* **80**, 1129-1134 (2006).
- [27] S. Axelrod, P. N. Sen, “Nuclear magnetic resonance spin echoes for restricted diffusion in an inhomogeneous field: Methods and asymptotic regimes”, *J. Chem. Phys.* **114**, 6878-6895 (2001).
- [28] M. Bossy, E. Gobet, and D. Talay, “A Symmetrized Euler Scheme for an Efficient Approximation of Reflected Diffusions”, *J. Appl. Prob.* **41**, 877-889 (2004).
- [29] K. Burdzy and Z.-Q. Chen, “Discrete approximations to reflected Brownian motion”, *Ann. Probab.* **36**, 698-727 (2008).
- [30] Z.-Q. Chen, “On reflecting diffusion processes and Skorokhod decompositions”, *Probab. Theory Related Fields* **94** 281-351 (1993).
- [31] M. Fukushima, Y. Oshima, and M. Takeda, “Dirichlet Forms and Symmetric Markov Processes”, de Gruyter Studies in Math., vol. 19 (Walter de Gruyter, Berlin and Hawthorne, NY, 1994).
- [32] D. S. Grebenkov, “Partially Reflected Brownian Motion: A Stochastic Approach to Transport Phenomena”, in “Focus on Probability Theory”, Ed. L. R. Velle, pp. 135-169 (Nova Science Publishers, 2006).

- [33] G. B. Arfken and H. J. Weber, *Mathematical methods for physicists*, 5th Ed. (Academic press, San Diego, 2001).
- [34] J. Crank, *The Mathematics of Diffusion*, 2nd Ed. (Clarendon, Oxford, 1975).
- [35] H. S. Carslaw and J. C. Jaeger, *Conduction of Heat in Solids*, 2nd Ed. (Clarendon, Oxford, 1959).
- [36] P. T. Callaghan, *Principles of Nuclear Magnetic Resonance Microscopy* (Clarendon Press, Oxford, 1991).
- [37] H. C. Torrey, “Bloch Equations with Diffusion Terms”, *Phys. Rev.* **104**, 563-565 (1956).
- [38] E. R. Weibel, *The Pathway for Oxygen. Structure and Function in the Mammalian Respiratory System* (Harvard University Press, Cambridge, Massachusetts and London, England, 1984).
- [39] M. P. Stone, K. R. Stone, P. Ingram, D. D. Mickey, and D. F. Paulson, “Scanning and Transmission Electron Microscopy of Human Prostatic Acinar Cells”, *Urolog. Res.* **5**, 185-200 (1977).
- [40] A. Plassais, M.-P. Pomiès, N. Lequeux, J.-P. Korb, D. Petit, F. Barberon, and B. Bresson, “Microstructure evolution of hydrated cement pastes”, *Phys. Rev. E* **72**, 041401 (2005).
- [41] R. L. Kleinberg, “Well logging overview”, *Conc. Magn. Reson. A* **13**, 342 (2001).
- [42] R. de Levie, “The Influence of Surface Roughness of Solid Electrodes on Electrochemical Measurements”, *Electrochimica Acta* **10**, 113-130 (1965).
- [43] M.-O. Coppens, “The effect of fractal surface roughness on diffusion and reaction in porous catalysts: from fundamentals to practical applications”, *Catalyst Today* **53**, 225-243 (1999).
- [44] M. E. Muller, “Some Continuous Monte Carlo Methods for the Dirichlet Problem”, *Annals Math. Statist.* **27**, 569-589 (1956).
- [45] S. Torquato, I. C. Kim, “Efficient simulation technique to compute effective properties of heterogeneous media”, *Appl. Phys. Lett.* **55**, 1847 (1989).
- [46] L. H. Zheng, Y. C. Chiew, “Computer simulation of diffusion-controlled reactions in dispersions of spherical sinks”, *J. Chem. Phys.* **90**, 322-327 (1989).
- [47] P. Ossadnik, “Multiscaling Analysis of Large-Scale Off-Lattice DLA”, *Physica A* **176**, 454 (1991).
- [48] B. Mandelbrot, *The Fractal Geometry of Nature* (San Francisco, Freeman, 1982).
- [49] J. Feder, *Fractals* (New York, Plenum Press, 1988).
- [50] B. Sapoval, *Les Fractales* (Paris, Aditech, 1990).

- [51] J.-F. Gouyet, *Physics and Fractal Structures* (Springer, 1996).
- [52] D. S. Grebenkov, A. A. Lebedev, M. Filoche, B. Sapoval, “Multifractal Properties of the Harmonic Measure on Koch Boundaries in Two and Three Dimensions”, *Phys. Rev. E* **71**, 056121 (2005).
- [53] J. B. Garnett and D. E. Marshall, *Harmonic Measure* (Cambridge University Press, 2005).
- [54] B. Duplantier, “Two-Dimensional Copolymers and Exact Conformal Multifractality”, *Phys. Rev. Lett.* **82**, 880 (1999).
- [55] B. Duplantier, “Harmonic Measure Exponents for Two-Dimensional Percolation”, *Phys. Rev. Lett.* **82**, 3940 (1999).
- [56] B. Duplantier, “Conformally Invariant Fractals and Potential Theory”, *Phys. Rev. Lett.* **84**, 1363 (1999).
- [57] N. G. Makarov, “On the distortion of boundary sets under conformal mappings”, *Proc. London Math. Soc.* **51**, 369 (1985).
- [58] T. H. Wolff, in *Essays on Fourier Analysis in Honor of Elias M. Stein*, Princeton Math. Ser., Vol. 42 (Princeton University Press, Princeton, N. J., 1995), pp. 321-384.
- [59] D. S. Grebenkov, “What Makes a Boundary Less Accessible”, *Phys. Rev. Lett.* **95**, 200602 (2005).
- [60] D. S. Grebenkov, M. Filoche, B. Sapoval, “Spectral Properties of the Brownian Self-Transport Operator”, *Eur. Phys. J. B* **36**, 221-231 (2003).
- [61] M. Filoche, B. Sapoval, “Can One Hear the Shape of an Electrode? II. Theoretical Study of the Laplacian Transfer”, *Eur. Phys. J. B* **9**, 755-763 (1999).
- [62] B. Sapoval, J. S. Andrade Jr, A. Baldassari, A. Desolneux, F. Devreux, M. Filoche, D. S. Grebenkov, S. Russ, “New Simple Properties of a Few Irregular Systems”, *Physica A* **357**, 1-17 (2005).
- [63] D. S. Grebenkov, “Scaling Properties of the Spread Harmonic Measures”, *Fractals* **14**, 231-243 (2006).
- [64] R. D. Armstrong and R. A. Burnham, “The Effect of Roughness on the Impedance of the Interface Between a Solid Electrolyte and a Blocking Electrode”, *J. Electroanal. Chem.* **72**, 257-266 (1976).
- [65] L. Nyikos and T. Pajkossy, “Fractal Dimension and Fractional Power Frequency-Dependent Impedance of Blocking Electrodes”, *Electrochem. Acta* **30**, 1533-1540 (1985).
- [66] T. C. Halsey and M. Leibig, “The Double Layer Impedance at a Rough Surface: Theoretical Results”, *Annals of Physics* **219**, 109-147 (1992).

- [67] B. Sapoval, R. Gutfraind, P. Meakin, M. Keddam, and H. Takenouti, “Equivalent-Circuit, Scaling, Random-Walk Simulation, and an Experimental Study of Self-Similar Fractal Electrodes and Interfaces”, *Phys. Rev. B* **48**, 3333-3344 (1993).
- [68] P. Levitz, D. S. Grebenkov, M. Zinsmeister, K. Kolwankar, B. Sapoval, “Brownian flights over a fractal nest and first passage statistics on irregular surfaces”, *Phys. Rev. Lett.* **96**, 180601 (2006).
- [69] P.-G. de Gennes, “Transfert d’excitation dans un milieu aléatoire”, *C. R. Acad. Sci. Paris, Sér. II* **295**, 1061 (1982).
- [70] P. Levitz, “Random flights in confining interfacial systems”, *J. Phys. Condens. Matter* **17**, S4059 (2005).
- [71] B. Duplantier, “Can One ‘Hear’ the Thermodynamics of a (Rough) Colloid?” *Phys. Rev. Lett.* **66**, 1555 (1991).
- [72] O. Bénichou, M. Coppey, M. Moreau, P. H. Suet, and R. Voituriez, “Averaged residence times of stochastic motions in bounded domains”, *Europhys. Lett.* **70**, 42 (2005).
- [73] P. Levitz and J.-P. Korb, “Probing glass transition of clay colloids by NMR relaxometry - Interplay between fluid Brownian dynamics and particle jamming”, *Europhys. Lett.* **70**, 684 (2005).
- [74] G. F. Froment and K. B. Bischoff, *Chemical reactor analysis and design* (John Wiley & Sons, New York, 1990).
- [75] N. Epstein, *Fouling Science and Technology*, ed. by L. F. Melo, and C. A. Bernardo, *Proc. of the NATO Advanced Study Institute on Advances in Fouling Science and Technology*, 1987 (Portugal, Kluwer Academic Publishers: Dordrecht, The Netherlands, 1988), p. 15.
- [76] T. J. Pricer, M. J. Kushner, and R. C. Alkire, “Monte Carlo Simulation of the Electrodeposition of Copper II. Acid Sulfate Solution with Blocking Additive”, *J. Electrochem. Soc.* **149**, C406-C412 (2002).
- [77] J. M. DeSesso and C. F. Jacobson, “Anatomical and physiological parameters affecting gastrointestinal absorption in humans and rats”, *Food and Chemical Toxicology*, **39** 209-228 (2001).
- [78] R. G. Yan, G. Z. Yan, and B. H. Yang, *Trans. Eng. Comp. and Technol.* **11**, 255-258 (2006).
- [79] A. Farhadi, A. Banan, J. Fields, and A. Keshavarzian, “Intestinal barrier: An interface between health and disease”, *J. Gastroenterol. Hepatol.* **18**, 479-497 (2003).
- [80] C. H. Bartholomew, “Mechanisms of catalyst deactivation”, *Applied Catalysis A-General* **212**, 17-60 (2001).
- [81] J. S. Andrade Jr., E. A. A. Henrique, M. P. Almeida, and M. H. A. S. Costa, “Heat transport through rough channels”, *Physica A* **339**, 296-310 (2004).

- [82] J. P. Meyer, and H. Van der Vyver, “Heat Transfer Characteristics of a Quadratic Koch Island Fractal Heat Exchanger”, *Heat Transfer Engineering* **26**, 22-29 (2005).
- [83] A. Helalizadeh, H. Müller-Steinhagen, and M. Jamialahmadi, “Application of fractal theory for characterisation of crystalline deposits”, *Chem. Eng. Sci.* **61**, 2069-2078 (2006).
- [84] M. Filoche, D. S. Grebenkov, J. S. Andrade Jr., B. Sapoval, “The Role of Geometry in the Passivation of Irregular Surfaces Accessed by Diffusion”, *Proc. Natl. Acad. Sci.* **105**, 7636-7640 (2008).
- [85] B. Sapoval, M. H. A. S. Costa, J. S. Andrade, M. Filoche, “Laplacian Transport Towards Partially Passivated 2D Irregular Interfaces: A Conjecture Extension of the Makarov Theorem” *Fractals* **12**, 381-387 (2004).
- [86] M. Felici, M. Filoche, and B. Sapoval, “Diffusional screening in the human pulmonary acinus”, *J. Appl. Physiol.* **94**, 2010-2016 (2003).
- [87] M. Felici, B. Sapoval, and M. Filoche, “Renormalized Random Walk Study of Oxygen Absorption in the Human Lung”, *Phys. Rev. Lett.* **92**, 068101 (2004).
- [88] D. S. Grebenkov, M. Filoche, B. Sapoval, M. Felici, “Diffusion-Reaction in Branched Structures: Theory and Application to the Lung Acinus”, *Phys. Rev. Lett* **94**, 050602 (2005).
- [89] H. Kitaoka, S. Tamura, and R. Takaki, “A three-dimensional model of the human pulmonary acinus”, *J. Appl. Physiol.* **88**, 2260-2268 (2000).
- [90] D. S. Grebenkov, G. Guillot, B. Sapoval, “Restricted Diffusion in a Model Acinar Labyrinth by NMR. Theoretical and Numerical Results”, *J. Magn. Reson.* **184**, 143-156 (2007).
- [91] D. S. Grebenkov, G. Guillot, “Numerical MRI of the translational diffusion in branching three-dimensional labyrinths of a model pulmonary acinus”, *MAGMA* **18**, S128 (2005).
- [92] S. D. Stoller, W. Happer, and F. J. Dyson, “Transverse spin relaxation in inhomogeneous magnetic fields”, *Phys. Rev. A* **44**, 7459-7477 (1991).
- [93] M. D. Hürlimann, K. G. Helmer, T. M. de Swiet, P. N. Sen, and C. H. Sotak, “Spin Echoes in a Constant Gradient and in the Presence of Simple Restriction”, *J. Magn. Reson. A* **113**, 260-264 (1995).
- [94] D. Habib, D. S. Grebenkov, G. Guillot, “Gas diffusion in a pulmonary acinus model: experiments with hyperpolarized helium-3”, *Magn. Reson. Imaging* **26**, 1101-1113 (2008).
- [95] D. Habib, D. S. Grebenkov, G. Guillot, “Probing a model pulmonary acinus by NMR gas diffusion”, *Magn. Reson. Imag.* **25**, 560 (2007).
- [96] D. S. Grebenkov, G. Guillot, “NMR of diffusion in porous media: branched or disordered structure?”, *Magn. Reson. Imag.* **25**, 560 (2007).

- [97] P. N. Sen, “Time-dependent diffusion coefficient as a probe of geometry”, *Concepts Magn. Reson.* **23** A, 1-21 (2004).
- [98] S. Rodts and P. Levitz, “Time domain analysis: an alternative way to interpret PGSE experiment”, *Magn. Reson. Imag.* **19**, 465-467 (2001).
- [99] T. A. Witten and L. M. Sander, “Diffusion-Limited Aggregation, a Kinetic Critical Phenomenon”, *Phys. Rev. Lett.* **47**, 1400-1403 (1981).
- [100] T. C. Halsey, “Diffusion-limited aggregation: A model for pattern formation”, *Physics Today* **53**, 36-41 (2000).
- [101] O. G. Berg, R. B. Winter, and P. H. von Hippel, “Diffusion-driven mechanisms of protein translocation on nucleic acids. 1. Models and theory”, *Biochemistry* **20**, 6929 (1981).
- [102] D. L. Kramer and R. L. McLaughlin, “The Behavioral Ecology of Intermittent Locomotion”, *Am. Zool.* **41**, 137-153 (2001).
- [103] K. R. McCall, D. L. Johnson, and R. A. Guyer, “Magnetization evolution in connected pore systems,” *Phys. Rev. B* **44**, 7344-7355 (1991).
- [104] R. E. Jacob, G. Laicher, and K. R. Minard, “3D MRI of non-Gaussian ^3He gas diffusion in the rat lung”, *J. Magn. Reson.* **188**, 357-366 (2007).
- [105] D. A. Yablonskiy, A. L. Sukstanskii, J. C. Leawoods, D. S. Gierada, G. L. Bretthorst, S. S. Lefrak, J. D. Cooper, and M. S. Conradi, “Quantitative in vivo Assessment of Lung Microstructure at the Alveolar Level with Hyperpolarized ^3He Diffusion MRI”, *Proc. Nat. Acad. Sci.* **99**, 3111 (2002).
- [106] G. Guillot, D. Habib, J.M. Pérez-Sanchez, L. del Puerto Nevado, S. Pérez-Rial, I. Rodriguez, J. Ruiz-Cabello, and G. Peces-Barba, “Influence of diffusion gradient intensity on the ADC value with HP ^3He in an animal model”, in *Proc. of ESMRMB*, # 592 (Valencia, Spain, 2008).
- [107] E. E. Sigmund, H. Cho, P. Chen, S. Byrnes, Y.-Q. Song, X. E. Guo, and T. R. Brown, “Diffusion-Based MR Methods for Bone Structure and Evolution”, *Magn. Reson. Med.* **59**, 28-39 (2008).
- [108] P. D. Watson and F. S. Grodins, “An Analysis of the Effects of the Interstitial Matrix on Plasma-Lymph Transport”, *Microvasc. Res.* **16**, 19-41 (1978).
- [109] K. Aukland, R. K. Reed, “Interstitial-Lymphatic Mechanisms in the Control of Extracellular Fluid Volume”, *Physiol. Rev.* **73**, 1-78 (1993).
- [110] D. G. Taylor, J. L. Bert, B. D. Bowen, “A Mathematical Model of Interstitial Transport I. Theory”, *Microvasc. Res.* **39**, 253 (1990).
- [111] J. R. Levick, “A Two-Dimensional Morphometry-Based Model of Interstitial and Transcapillary Flow in Rabbit Synovium”, *Q. J. Exp. Physiol.* **76**, 905 (1991).

- [112] A. G. Ogston, "The spaces in a uniform random suspension of fibers", *Trans. Faraday Soc.* **54**, 1754-1757 (1958).
- [113] D. S. Tsai and W. Strieder, "Effective conductivities of random fiber beds", *Chem. Eng. Commun.* **40**, 207-218 (1986).
- [114] R. J. Phillips, W. M. Deen, and J. F. Brady, "Hindered transport in fibrous membranes and gels - Effect of solute size and fiber configuration", *J. Coll. Int. Sci.* **139**, 363-373 (1990).
- [115] M. M. Tomadakis and T. J. Robertson, "Pore size distribution, survival probability, and relaxation time in random and ordered arrays of fibers", *J. Chem. Phys.* **119**, 1741-1749 (2003).
- [116] K. Benirschke, P. Kaufmann, and R. Baergen, *The Pathology of the Human Placenta*, Fourth Edition (Springer 2000).
- [117] T. M. Mayhew, "Allometric studies on growth and development of the human placenta: growth of tissue compartments and diffusive conductances in relation to placental volume and fetal mass", *J. Anat.* **208**, 785-794 (2006).
- [118] D. S. Grebenkov, "Laplacian Eigenfunctions in NMR I. A Numerical Tool", *Concepts Magn. Reson.* **32A**, 277-301 (2008).
- [119] D. S. Grebenkov, "Laplacian Eigenfunctions in NMR II. Theoretical Advances", *Concepts Magn. Reson. A* (to be published, 2009).
- [120] A. Caprihan, L. Z. Wang, and E. Fukushima, "A Multiple-Narrow-Pulse Approximation for Restricted Diffusion in a Time-Varying Field Gradient", *J. Magn. Reson. A* **118**, 94-102 (1996).
- [121] P. T. Callaghan, "A Simple Matrix Formalism for Spin Echo Analysis of Restricted Diffusion under Generalized Gradient Waveforms", *J. Magn. Reson.* **129**, 74-84 (1997).
- [122] A. V. Barzykin, "Exact Solution of the Torrey-Bloch Equation for a Spin Echo in Restricted Geometries", *Phys. Rev. B* **58**, 14171-14174 (1998).
- [123] A. V. Barzykin, "Theory of Spin Echo in Restricted Geometries under a Step-wise Gradient Pulse Sequence", *J. Magn. Reson.* **139**, 342-353 (1999).
- [124] D. S. Grebenkov, "Multiple correlation function approach to study the restricted diffusion under arbitrary magnetic field", *Magn. Reson. Imag.* **25**, 559 (2007).
- [125] H. Y. Carr and E. M. Purcell, "Effects of diffusion on free precession in NMR experiments", *Phys. Rev.* **94**, 630-638 (1954).
- [126] D. S. Grebenkov, "Multiexponential attenuation of the CPMG spin echoes due to a geometrical confinement", *J. Magn. Reson.* **180**, 118-126 (2006).
- [127] E. O. Stejskal and J. E. Tanner, "Spin diffusion measurements - spin echoes in the presence of a time-dependent field gradient", *J. Chem. Phys.* **42**, 288-292 (1965).

- [128] D. S. Grebenkov, “Analytical solution for restricted diffusion in circular and spherical layers under inhomogeneous magnetic fields”, *J. Chem. Phys.* **128**, 134702 (2008).
- [129] B. Robertson, “Spin-echo decay of spins diffusion in a bounded region”, *Phys. Rev.* **151**, 273-277 (1966).
- [130] C. H. Neuman, “Spin echo of spins diffusion in a bounded medium”, *J. Chem. Phys.* **60**, 4508-4511 (1974).
- [131] P. P. Mitra, P. N. Sen, L. M. Schwartz, and P. Le Doussal, “Diffusion propagator as a probe of the structure of porous media”, *Phys. Rev. Lett.* **68**, 3555 (1992).
- [132] P. P. Mitra, P. N. Sen, and L. M. Schwartz, “Short-time behavior of the diffusion coefficient as a geometrical probe of porous media”, *Phys. Rev. B* **47**, 8565-8574 (1993).
- [133] T. M. de Swiet and P. N. Sen, “Decay of nuclear magnetization by bounded diffusion in a constant field gradient”, *J. Chem. Phys.* **100**, 5597-5604 (1994).
- [134] D. S. Grebenkov, “Multiple Correlation Function Approach: Rigorous Results for Simple Geometries”, *Diff. Fundam.* **5**, 1-34 (2007).
- [135] D. S. Grebenkov, “Nuclear Magnetic Resonance Restricted Diffusion between Parallel Planes in a Cosine Magnetic Field: An Exactly Solvable Model”, *J. Chem. Phys.* **126**, 104706 (2007).
- [136] L. J. Zielinski and P. N. Sen, “Relaxation of nuclear magnetization in a nonuniform magnetic field gradient and in a restricted geometry”, *J. Magn. Reson.* **147**, 95-103 (2000).
- [137] T. M. de Swiet and P. N. Sen, “Time dependent diffusion coefficient in a disordered medium”, *J. Chem. Phys.* **104**, 206-209 (1996)
- [138] D. S. Grebenkov, “Residence times and other functionals of reflected Brownian motion”, *Phys. Rev. E* **76**, 041139 (2007).
- [139] N. Agmon, “Residence times in diffusion processes”, *J. Chem. Phys.* **81**, 3644 (1984).
- [140] K. R. Brownstein and C. E. Tarr, “Importance of Classical Diffusion in NMR Studies of Water in Biological Cells”, *Phys. Rev. A* **19**, 2446-2453 (1979).
- [141] R. Zwanzig and A. Szabo, “Time dependent rate of diffusion-influenced ligand binding to receptors on cell surfaces”, *Biophys. J.* **60**, 671-678 (1991).
- [142] O. V. Bychuk and B. O’Shaughnessy, “Anomalous Diffusion at Liquid Surfaces”, *Phys. Rev. Lett.* **74**, 1795-1798 (1995).
- [143] S. Stapf, R. Kimmich, and R.-O. Seitter, “Proton and Deuteron Field-Cycling NMR Relaxometry of Liquids in Porous Glasses: Evidence for Lévy-Walk Statistics”, *Phys. Rev. Lett.* **75**, 2855-2858 (1995).

- [144] O. Bénichou, C. Loverdo, M. Moreau, and R. Voituriez, “Two-dimensional intermittent search processes: An alternative to Levy flight strategies”, *Phys. Rev. E* **74**, 020102R (2006).
- [145] R. B. Platte and A. T. Driscoll, “Computing eigenmodes of elliptic operators using radial basis functions”, *Comput. Math. App.* **48**, 561-576 (2004).
- [146] C. J. S. Alves and C. S. Chen, “A new method of fundamental solutions applied to nonhomogeneous elliptic problems”, *Adv. Comp. Math.* **23**, 125-142 (2005).
- [147] T. Betcke and L. N. Trefethen “Reviving the Method of Particular Solutions”, *SIAM Reviews* **47**, 469-491 (2005).
- [148] L. Banjai, “Eigenfrequencies of fractal drums”, *J. Comput. Appl. Math.* **198**, 1-18 (2007).
- [149] S. Russ, B. Sapoval, and O. Haeblerlé, “Irregular and fractal resonators with Neumann boundary conditions: Density of states and localization”, *Phys. Rev. E* **55**, 1413 (1997).
- [150] S. Russ and B. Sapoval, “Increased damping of irregular resonators”, *Phys. Rev. E* **65**, 036614 (2002)
- [151] S. Félix, M. Asch, M. Filoche, and B. Sapoval, “Localization and increased damping in irregular acoustic cavities”, *J. Sound and Vibr.* **299**, 965-976 (2007).
- [152] S. Redner, *A Guide to First-Passage Processes* (Cambridge University Press, Cambridge, England, 2001).
- [153] S. B. Lee, I. C. Kim, C. A. Miller, and S. Torquato, “Random-walk simulation of diffusion-controlled processes among static traps”, *Phys. Rev. B* **39**, 11833-11839 (1989).
- [154] G. H. Weiss, “Overview of theoretical models for reaction rates”, *J. Stat. Phys.* **42**, 3-36 (1986).
- [155] A. M. Berezhkovskii, D. J. Bicout, G. H. Weiss, “Target and trapping problems - From the ballistic to the diffusive regime”, *J. Chem. Phys.* **110**, 1112-1122 (1999).
- [156] M. Mulqueen, K. J. Stebe, and D. Blankschtein, “Dynamic Interfacial Adsorption in Aqueous Surfactant Mixtures - Theoretical Study”, *Langmuir* **17**, 5196 (2001).
- [157] S.-Y. Lin, K. McKeigue, and C. Maldarelli, “Diffusion-controlled surfactant adsorption studied by pendant drop digitization”, *AIChE J.* **36**, 1785 (1990).
- [158] J. M. Schurr, “The Role of Diffusion in Bimolecular Solution Kinetics”, *Biophys. J.* **10**, 700 (1970).
- [159] J. M. Schurr, “The Role of Diffusion in Enzyme Kinetic”, *Biophys. J.* **10**, 717 (1970).
- [160] H. C. Berg and E. M. Purcell, “Physics of chemoreception”, *Biophys. J.* **20**, 193 (1977).

- [161] C. Ybert and J. M. di Meglio, “Study of Protein Adsorption by Dynamic Surface Tension Measurements - Diffusive Regime”, *Langmuir* **14**, 471 (1998).
- [162] E. Leikina, I. Markovic, L. V. Chernomordik, and M. M. Kozlov, “Delay of Influenza Hemagglutinin Refolding into a Fusion-Competent Conformation by Receptor Binding: A Hypothesis”, *Biophys. J.* **79**, 1415 (2000).
- [163] T. Chou and M. R. D’Orsogna, “Multistage adsorption of diffusing macromolecules and viruses”, *J. Chem. Phys.* **127**, 105101 (2007).
- [164] R. Pettersson, “Penalization schemes for reflecting stochastic differential equations”, *Bernoulli* **3**, 403-414 (1997).
- [165] Q. Liu and O. V. Vasilyev, “A Brinkman penalization method for compressible flows in complex geometries”, *J. Comput. Phys.* **227**, 946-966 (2007).
- [166] M. Sarracanie, X. Maître, A. Caluch, R. Santarelli, R.-M. Dubuisson, L. Darrasse, B. Louis, R. Fodil, E. Boriassse, F. Marsolat, D. S. Grebenkov, M. Filoche, B. Sapoval, G. Caillibotte, G. Apiou, D. Isabey, E. Durand, and J. Bittoun, “Assessment of hyperpolarised helium-3 MRI for aerosol deposition in the lungs”, Proceedings of the 25th Annual Meeting of the ESMRMB, # 959 (Valencia, Spain, 2008).
- [167] D. Habib, D. S. Grebenkov, G. Guillot, “Probing a model pulmonary acinus by NMR gas diffusion”, Proceedings of the 8th International Bologna Conference on Magnetic Resonance in Porous Media, p. 55 (Bologna, Italy, 2006).
- [168] D. Habib, D. S. Grebenkov, X. Maître, L. De Rochefort, E. Durand, G. Guillot, “Experimental study of gas diffusion in a pulmonary acinus model”, Proceedings of the Fourteenth ISMRM Meeting, # 1323 (Seattle, USA, 2006).